Dynamics of martensitic phase boundaries: discreteness, dissipation and inertia

Lev Truskinovsky * Anna Vainchtein †

October 19, 2007

Abstract

We study a fully inertial model of a martensitic phase transition in a one-dimensional crystal lattice with long-range interactions. The model allows one to represent a broad range of dynamic regimes, from underdamped to overdamped. We systematically compare the discrete model with its various continuum counterparts including elastic, viscoelastic and viscosity-capillarity models. Each of these models generates a particular kinetic relation which links the driving force with the phase boundary velocity. We find that the viscoelastic model provides an upper bound for the critical driving force predicted by the discrete model, while the viscosity-capillarity model delivers a lower bound. We show that at near-sonic velocities, where inertia dominates dispersion, both discrete and continuum models behave qualitatively similarly. At small velocities, and in particular, near the depinning threshold, the discreteness prevails and predictions of the continuum models cannot be trusted.

1 Introduction

Proper martensitic phase transitions in crystals represent largely mechanical phenomena. They are associated with softening of an elastic modulus and generate spontaneous deformation which transforms a high-symmetry parent lattice into a low-symmetry ferroelastic phase. The latter is characterized by several stable variants (twins) corresponding to different atomic arrangements which are structurally fully identical. During these

*Laboratoire de Mechanique des Solides, CNRS-UMR 7649, Ecole Polytechnique, 91128, Palaiseau, France

†Department of Mathematics, University of Pittsburgh, Pittsburgh, PA 15260

transformations both elasticity and dynamics play a crucial role and a component of the macroscopic strain is used as the order parameter [11, 14, 19, 17].

Materials undergoing martensitic phase transitions are known to exhibit damping and hysteresis under cyclic loading [15, 13]. The task of optimizing the corresponding energy dissipation through microstructural and compositional selection presents an important technological challenge. It is well understood that the energy is dissipated due to propagation of phase and twin boundaries. The dissipation takes place inside the atomically sharp transition zones and must be modeled by lattice theories. Adequate molecular dynamical models are available, but due to the necessity of resolving a large number of nonlinear degrees of freedom, they are analytically opaque and can be used only for numerical experiments. The transition zones can also be modeled at the macroscopic level, as jump discontinuities. However, since elastodynamics does not provide any information about the rate of the transformation, the system of jump conditions has to be closed phenomenologically (e.g. [25, 1, 12]). Various quasicontinuum augmentations of classical elasticity, incorporating dispersion and dissipation mechanisms and providing the desired closure, have been proposed in the literature, albeit without an explicit link to the underlying discrete theory (see the reviews [26, 5]).

In this paper we establish such a link by studying dynamics of a phase boundary associated with a *prototypical* martensitic transformation in a model lattice. To obtain analytical results we consider the simplest nonlocal extension of the one-dimensional mass-spring system proposed in [23, 22]. The discreteness is viewed as representing either atomic structure or a system of periodically placed obstacles; the nonlocality of the model is intended to mimic three-dimensional effects. The martensitic phase transition is modeled as the bistability of the springs connecting nearest neighbors. In addition, the model incorporates inertial and dissipative terms, which allows one to cover the whole range of dynamic regimes, from underdamped to overdamped.

To reconstruct the effect of lattice-induced dispersion on the kinetic behavior of the martensitic phase boundaries, we introduce a dimensionless parameter δ, characterizing the degree of discreteness. We then consider two limits: when the model is strongly discrete and when it is almost continuous. In the continuum limit $\delta \to 0$ we recover the classical elasticity theory which is now supplied with a particular kinetic relation for the phase discontinuities. This relation depends on the details of the limiting procedure, in particular, on the asymptotic behavior of the parameters representing dissipative properties of the model. By expanding the governing equations at small δ we recover various quasicontinuum regularizations of the classical theory, including the ones which have been previously advanced on the phenomenological grounds. In particular, we formally qualify the asymptotic limits bringing in the viscoelasticity model [16] and the viscosity-capillarity model [21, 24].

To recover the kinetic relation, we consider an isolated phase boundary driven by

the conditions at infinity and solve the associated traveling wave problem. This problem can be viewed as a nonlinear eigenvalue problem for the phase boundary velocity. The conditions at infinity define the driving force, and we search for a functional relation between the driving force and the velocity ensuring that the eigenvalue problem has a solution. Using the partial linearity of the discrete model we obtain such a relation in the closed form and compare it to the viscoelastic and viscosity-capillarity counterparts, corresponding for the same values of the microscopic parameters.

We find that at near-sonic velocities, when inertial and dissipative effects dominate dispersion, the kinetic relations in all three models have the same asymptotic structure. On the phenomenological level, the ensuing kinetic relation corresponds to the maximum dissipation criterion which can also be derived formally from the viscoelastic model. At small velocities the kinetic relations in discrete and continuum models are quite different. The discrete model predicts lattice trapping: a phase boundary cannot move until the driving force reaches a certain nonzero threshold, which we call the Peierls driving force by analogy with dislocation theory (e.g [10]). The magnitude of the Peierls force is largely exaggerated by the viscoelastic model and is completely missed by the viscosity-capillarity model. This leads to vastly different overdamped limits which can be interpreted as the zoom in on the kinetic curves in the region where the inertial effects are negligible. In general, our calculations show that viscosity-capillarity model provides a lower bound for the discrete kinetics, while the viscoelasticity model delivers an upper bound. When viscous damping increases, the range of velocities where the three models are qualitatively similar broadens although the the quantitative thresholds remain different.

As we have implied above, viscosity-capillarity model provides a good representation of discrete kinetics in the regimes of high damping and large inertia. The approximation becomes progressively worse as viscosity decreases. At zero viscosity, the model becomes even qualitatively incorrect as it predicts zero dissipation in the whole range of velocities up to the sonic limit. In contrast, the discrete model yields nonzero macroscopic dissipation even in the Hamiltonian limit which is then caused by radiative damping [30]. In general, the deficiencies of the viscosity-capillarity model point to the urgent need for the development of other quasicontinuum approximations, adequately reproducing the dispersive properties of the discrete model in the physically relevant underdamped regimes. Different proposals in this direction can be found in [9, 31, 4].

The paper is organized as follows. In Section 2 we introduce the discrete model, specify the main dimensionless parameters and determine the exact scaling in the regimes of interest. Various continuum and quasicontinuum approximations are derived and studied in Section 3. In Section 4 we give the full solution of the discrete problem and study several important limiting cases including the overdamped and Hamiltonian regimes. We then specialize the discrete model to the case of only nearest and next-to-nearest neighbor interactions (NNN model) and perform a systematic quantitative case-study of this

example. A detailed comparison of the discrete and continuum kinetic relations emerging in this benchmark problem is presented in Section 5. The final Section 6 summarizes our conclusions.

2 The model

We begin by introducing the discrete model, formulating the problem in dimensionless form and specifying the asymptotic regimes studied in detail in the subsequent sections.

2.1 Elastic energy

Consider a one-dimensional lattice, or chain, comprised of isolated point masses connected by springs. Each mass interacts with its q neighbors on each side. If $u_n(t)$ is the displacement of the nth mass, the sum of kinetic and potential energies of the chain can be written as

$$\mathcal{E} = \varepsilon \sum_{n=-\infty}^{\infty} \left[\frac{\rho \dot{u}_n^2}{2} + \sum_{p=1}^{q} p\phi_p \left(\frac{u_{n+p} - u_n}{p\varepsilon} \right) \right]. \tag{1}$$

Here the function $\phi_p(w)$ defines the potential of the elastic interaction between pth nearest neighbors, ε is the reference interparticle distance and ρ is the constant mass density.

The next step is to specify the interparticle potentials ϕ_p. We recall that in order to support a proper martensitic phase transition, the macroscopic elastic energy of the material must be at least bistable. The macroscopic energy can be derived from the microscopic potentials

$$\phi(w) = \sum_{p=1}^{q} p\phi_p(w). \tag{2}$$

In the interest of analytical simplicity we assume that the function $\phi(w)$ is biquadratic:

$$\phi(w) = \begin{cases} \frac{1}{2}Ew^2, & w \le w_c \\ \frac{1}{2}E(w-\Delta)^2 + \Delta E\left(w_c - \frac{\Delta}{2} \right), & w \ge w_c, \end{cases} \tag{3}$$

where E is the macroscopic elastic modulus and Δ is the macroscopic transformation strain. The macroscopic stress-strain relation is then (see Fig. 1)

$$\hat{\sigma}(w) = \phi'(w) = \sum_{p=1}^{q} p\phi_p'(w) = E(w - \Delta\theta(w - w_c)). \tag{4}$$

The simplest way to secure the desired macroscopic response is to assume that in the

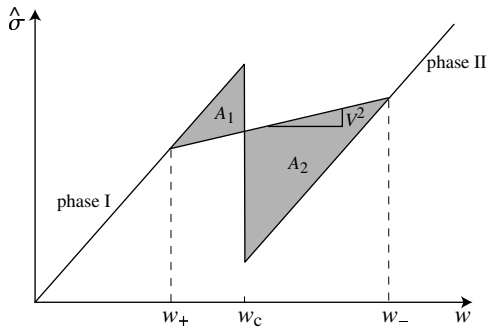

Figure 1: The bilinear stress-strain curve. The driving force $G = A_2 - A_1$ equals the difference between the two shaded areas.

micro-model the nearest-neighbor potential is biharmonic:

$$\phi_1(w) = \begin{cases} \frac{1}{2}\mu_1 w^2, & w \le w_c \\ \frac{1}{2}\mu_1 (w-a)^2 + a\mu_1 \left(w_c - \frac{a}{2} \right), & w \ge w_c, \end{cases} \tag{5}$$

while the long-range potentials are harmonic:

$$\phi_p(w) = \frac{1}{2} p \mu_p w^2, \quad p = 2, ..., q. \tag{6}$$

Here μ_p, $p = 1, \ldots, q$, are the microscopic elastic moduli, $a > 0$ is the microscopic transformation strain and w_c is the critical value of strain separating in (5) the two regions of convexity (two phases). The compatibility between the microscopic and macroscopic models requires that

$$E = \sum_{p=1}^{q} p^2 \mu_p \tag{7}$$

and

$$\Delta = a\mu_1 / E. \tag{8}$$

The microscopic moduli must ensure that $E > 0$ and that the the transformation strain is positive. Additional constraints on μ_p which guarantee stability in the discrete problem will be introduced later.

We remark that, in statics, the ensuing discrete model can be alternatively characterized as an Ising model with elastic wells. Indeed, the double-well potential, describing nearest-neighbor interactions (3), generates a spin-like variable, while the harmonic potentials (6) for next-to-nearest neighbors and beyond ensure that these "spins" interact. If the quadratic wells in (3) are replaced by the infinitely steep walls located at ± 1 ($\mu_1 \to \infty$), the static problem reduces exactly to the (nonlocal) Ising model.

2.2 Dissipation

In view of the fact that the model deals with only few generalized coordinates representing potentially much more complex phenomena at the microscale (for instance, it does not resolve electronic degrees of freedom), it is natural to conclude that the above Hamiltonian formulation is oversimplified and to include some dissipation already at the microscale.

Since we are aiming at the simplest prototypical formulation, we assume that the dissipation is linear, which means that the corresponding Rayleigh function is quadratic. While different assumptions can be made in this respect, we assume that the dissipation is viscous and that it comes from the viscoelasticity of the nearest-neighbor "springs". We must therefore supplement in the governing equations the elastic force between the nearest neighbors,

$$f_1^{(1)}(w) = \phi_1'(w),$$

by a second additive component representing the viscous force. We write it in the form

$$f_1^{(2)}(\dot{w}) = \xi \dot{w},$$

where $\xi > 0$ is the viscosity coefficient. The resulting dynamic equations can be written as

$$\rho \ddot{u}_n = \frac{1}{\varepsilon} \sum_{p=1}^{q} \left[\phi_p' \left(\frac{u_{n+p} - u_n}{p\varepsilon} \right) - \phi_p' \left(\frac{u_n - u_{n-p}}{p\varepsilon} \right) + \frac{\xi}{\varepsilon} \left(\dot{u}_{n+1} - 2\dot{u}_n + \dot{u}_{n-1} \right) \right]. \tag{9}$$

It will be convenient to rewrite equations (9) in terms of strains

$$w_n = \frac{u_n - u_{n-1}}{\varepsilon}. \tag{10}$$

Using our specific assumptions regarding the microscopic elastic potentials, we obtain

$$\begin{aligned} &\rho\varepsilon^2 \ddot{w}_n - \sum_{|k-n| \le q} \mu_{k-n} w_k + \xi(2\dot{w}_n - \dot{w}_{n+1} - \dot{w}_{n-1}) \\ &= \mu_1 a[2\theta(w_n - w_c) - \theta(w_{n+1} - w_c) - \theta(w_{n-1} - w_c)]. \end{aligned} \tag{11}$$

where $\theta(w)$ is the unit step function incorporating all the nonlinearity of the problem.

2.3 Scaling

To clarify the role of different terms in the system (11), it is necessary to non-dimensionalize it. Elastic moduli and the critical strain can be normalized by the macroscopic parameters E and Δ defined in (7) and (8), respectively. This produces dimensionless parameters

$$D_p = -\frac{\mu_p}{E}, \quad \tilde{w}_c = \frac{w_c}{\Delta},$$

which are assumed to be of order one. In view of (7) parameters D_p are not independent and $D_1 = -1 - \sum_{p=2}^{q} p^2 D_p$. Note also that $D_1 < 0$, since both E and μ_1 are assumed to be positive.

There are two characteristic velocities in the problem: the macroscopic sound speed $c_s = \sqrt{E/\rho}$, and the microscopic relaxational velocity $c_* = \varepsilon E/\xi$. The ratio of these velocities gives a dimensionless parameter

$$W = \frac{c_s}{c_*} = \frac{\xi}{\sqrt{\rho E}\varepsilon},$$

which characterizes the relative importance of dissipation at the scale of the lattice. In particular, when $W \approx 0$, the discreteness-induced dispersion dominates dissipation and, when $W \to \infty$, the dispersion can be neglected.

To quantify the presence of inertia, we assume that there is a third characteristic velocity c defining the rate of the external macroscopic processes under consideration. The ratio of the characteristic speed c and the macroscopic sound speed c_s can be taken as the second dimensionless parameter,

$$V = \frac{c}{c_s} = c\sqrt{\frac{\rho}{E}}.$$

This parameter is fully macroscopic and represents the analog of Mach number in gas dynamics. When $V \approx 0$, inertia is negligible, and the motion can be viewed as quasistatic; the ensuing dynamics is also overdamped if additionally $W \neq 0$.

The next step is to link the macroscopic and microscopic scales. Suppose that the characteristic external length of the problem is L. This introduces another dimensionless parameter,

$$\delta = \frac{\varepsilon}{L},$$

which characterizes the relative role of discreteness, or dispersion, at the macroscale. More specifically, when $\delta \approx 0$ we obtain almost continuum case (small dispersion), while $\delta \approx 1$ defines the strongly discrete (large dispersion) limit.

To rewrite the main system of equations (11) in dimensionless form, we define the new variables

$$\tau = \frac{tc}{L}, \quad \tilde{u}_n = \frac{u_n}{\Delta L}, \quad \tilde{w}_n = \frac{w_n}{\Delta}, \quad \tilde{\phi}_p(\tilde{w}) = \frac{\phi_p(\Delta\tilde{w})}{E\Delta^2}, \quad \tilde{\mathcal{E}} = \frac{\mathcal{E}}{E\Delta^2 L}. \tag{12}$$

Omitting the tildes on the new variables, we obtain the following expression for the energy:

$$\mathcal{E} = \delta \sum_{n=-\infty}^{\infty} \left[\frac{V^2 \dot{u}_n^2}{2} + \sum_{p=1}^{q} p\phi_p\left(\frac{u_{n+p} - u_n}{p\delta} \right) \right]. \tag{13}$$

The normalized equations read

$$V^2\ddot{w}_n - \frac{1}{\delta^2}\sum_{|k-n|\le q} D_{k-n}w_n + \frac{WV}{\delta}(2\dot{w}_n - \dot{w}_{n+1} - \dot{w}_{n-1}) \\ = \frac{1}{\delta^2}[2\theta(w_n - w_c) - \theta(w_{n+1} - w_c) - \theta(w_{n-1} - w_c)]. \tag{14}$$

We reiterate that the essential dimensionless parameters are W, V and δ.

It is of interest to consider two main cases: infinitesimal δ and finite δ. At small δ one is tempted to replace the discrete model by a continuum counterpart. Several possibilities are considered in the paper:

Classical elasticity. In the limit $\delta \to 0$, with two other non-dimensional criteria fixed, we obtain classical elasticity theory which contains neither dispersion nor dissipation.

Viscoelasticity. If we assume that δ is small but finite, expand the governing equations (14) in δ, and keep only the linear terms, we obtain a viscoelastic model with the macroscopic viscosity given by $W_* = W\delta$. Alternatively, this approximation can be obtained by considering the limit $\delta \to 0$ and $W \to \infty$, with W_* remaining finite.

Viscosity-capillarity model. By expanding the governing equations (14) up to the second order in δ, we obtain the viscosity-capillarity model. This approximation preserves the competition between the dissipative terms and the dispersive terms, mimicking the original discreteness of the problem.

At each value of δ, finite or infinitesimal, it is instructive to perform a parametric study of the problem in the space of parameters V and W. The following limiting cases are of particular interest:

Hamiltonian limit: $W = 0$. In this case the microscopic dissipation is absent. The macroscopic dissipation, however, may still be possible due to energy tunneling from short to long waves. In the context of dynamics of defects, this phenomenon is known as radiative damping.

Static limit: $V = 0$. This case is of interest due to the phenomenon of lattice trapping. The study of this case is necessary for determining the depinning threshold (Peierls stress).

Overdamped limit: $V \to 0$, $W \to \infty$, $V_* = VW = c/c_*$. In this approximation one zooms in on the depinning bifurcation and encounters the phenomenon of rate-independent dissipation. Here the inertia is neglected and the main interplay is between dissipation and dispersion whose ratio enters the problem through the parameter V_*. Our quasilinear system converges in this limit to a semilinear system, equivalent to the Frenkel-Kontorova model.

2.4 Traveling waves

We are now in a position to specify the macroscopic problem which attaches a particular meaning to the parameter c. To find the kinetic relation it is natural to consider a steady motion of an isolated phase boundary. The corresponding solution of the governing equations (14) must have the form of a *discrete traveling wave*

$$w_n(\tau) = w(\eta),$$

where $\eta = (n\varepsilon - ct)/L = n\delta - \tau$. Without loss of generality, we can assume that

$$w(\eta) < w_c \quad \text{for } \eta > 0, \qquad w(\eta) > w_c \quad \text{for } \eta < 0. \tag{15}$$

In this case, phase II is behind the localized transformation zone and phase I is in front (see Fig. 1); at $\eta = 0$ we need to impose the condition

$$w(0) = w_c. \tag{16}$$

Under these assumptions the infinite system (14) reduces to a single advance-delay differential equation:

$$\begin{aligned} &V^2 w'' + \frac{1}{\delta^2} \sum_{|p| \le q} D_p w(\eta + p\delta) - \frac{WV}{\delta}(2w'(\eta) - w'(\eta + \delta) - w'(\eta - \delta)) \\ &= \frac{1}{\delta^2}[2\theta(\eta) - \theta(\eta + \delta) - \theta(\eta - \delta)]. \end{aligned} \tag{17}$$

Observe that this equation is now linear due to the known location of the phase boundary. To specify the external boundary conditions for the equation (17), we further assume that

$$w(\eta) \to w_\pm \quad \text{as } \eta \to \pm\infty, \tag{18}$$

where $w_\pm$ are the limiting strains which can not be prescribed independently. Their interdependence, which remains implicit until the equation (17) is solved, is the ultimate reason for the existence of a particular kinetic relation.

3 Continuum approximations

We begin with the study of a series of approximate continuum models justified by the smallness of the parameter δ.

3.1 Classical elasticity

We assume that in the limit $\delta \to 0$ all fields of interest are sufficiently smooth so that one can perform the Taylor expansions in δ. Define $u(x,\tau)$ as the continuum displacement field which satisfies $u(n\delta,\tau) = u_n(\tau)$. By expanding finite differences in (13) and taking the limit $\delta \to 0$, we obtain

$$\mathcal{E} = \int \left[\frac{V^2 u_\tau^2}{2} + \phi(u_x) \right] dx. \tag{19}$$

In dimensionless variables equations (9) reduces to

$$V^2 u_{\tau\tau} = (\hat{\sigma}(u_x))_x. \tag{20}$$

Here $u_\tau \equiv \partial u/\partial\tau$ is the macroscopic velocity field and $u_x \equiv \partial u/\partial x$ is the macroscopic strain. The dimensionless macroscopic stress-strain relation is given by

$$\hat{\sigma}(w) = \phi'(w) = w - \theta(w - w_c). \tag{21}$$

In this continuum framework phase boundaries are described by jump discontinuities which are not constrained by Eq. (20) and must be defined by the appropriate jump conditions. To formulate these conditions we denote by f_- and f_+ the values of $f(x)$ to the left and to the right of the interface, and introduce the notations $[\![f]\!] \equiv f_+ - f_-$ for the jump and $\{f\} \equiv (f_+ + f_-)/2$ for the average of f across the discontinuity. We first recall the straightforward Rankine-Hugoniot jump conditions which ensure the balance of mass and momentum:

$$[\![u_\tau]\!] + V[\![u_x]\!] = 0, \quad V[\![u_\tau]\!] + [\![\hat{\sigma}(u_x)]\!] = 0. \tag{22}$$

Both the physical motivation of the problem and the mathematical requirement of well-posedness point towards the necessity of an additional assumption regarding the positive definiteness of the rate of dissipation

$$\mathcal{R} = GV \geq 0, \tag{23}$$

where

$$G = [\![\phi]\!] - \{\hat{\sigma}(u_x)\}[\![u_x]\!] \tag{24}$$

is the configurational (driving) force, which can be interpreted geometrically as the difference between the two shaded areas in Fig. 1. In what follows we check that in the limit $\delta \to 0$ both the Rankine-Hugoniot jump conditions (22) and the entropy inequality (23) follow from the discrete theory. Moreover, we show that in the case of a phase boundary with $|V| < 1$, not only the sign of the driving force but also its magnitude are dictated by the discrete theory. This imposes a link between the limiting strains on both sides of the discontinuity and sets up a specific kinetic relation.

To put things into perspective, we recall that in one-dimensional nonlinear elastodynamics, represented by Eq.(20), the entropy inequality is sufficient for local uniqueness in the case of supersonic discontinuities (shock waves) satisfying the Lax condition $c_+ < V < c_-$, where $c_\pm$ are the values of the sound velocity in front and behind the discontinuity. In the case of subsonic phase boundaries, or *kinks*, the Lax condition is violated and the non-uniqueness persists unless the rate of entropy production is specified precisely (e.g. [26]). This is usually done phenomenologically, by imposing a *kinetic relation*, first introduced in [25]. One expects that a particular kinetic relation in the form $G = G(V)$ should follow from the discrete theory in the limit $\delta \to 0$, and we show that this is in fact the case.

Until the discrete problem is solved, the function $G(V)$ cannot be specified. However, some natural bounds can be easily obtained. Thus, for our piecewise linear material the admissible set for kinks with $0 < V < 1$ is illustrated in Fig. 2. One of the boundaries of this set corresponds to reversible kinks which satisfy the kinetic relation $G = 0$ [24]. Another boundary marks the maximum rate of dissipation $\mathcal{R}$ at a given V. In particular, the static kinks ($V = 0$) become maximally dissipative when the driving force reaches the spinodal threshold $G_s = 1/2$. The classical continuum theory, incorporating Eq. (20) for smooth motions and Rankine-Hugoniot jump conditions (22) plus the entropy inequality (23) for discontinuities, allows for arbitrary kinks in the shaded area shown in Fig. 2. This is a clear sign of degeneracy of the classical theory and the necessity of an independent closure condition.

In the next subsections we show that higher order quasicontinuum approximations, allowing the parameter δ to be small but finite, are free from this degeneracy and can be used as sources of the particular kinetic relations. Later in the paper the adequacy of such kinetic relations will be checked against the discrete benchmark.

3.2 Viscoelasticity

Keeping linear terms in δ as we Taylor expand Eq.(14), we obtain the following partial differential equation:

$$V^2 u_{\tau\tau} = (\hat{\sigma}(u_x) + W\delta V u_{x\tau})_x. \tag{25}$$

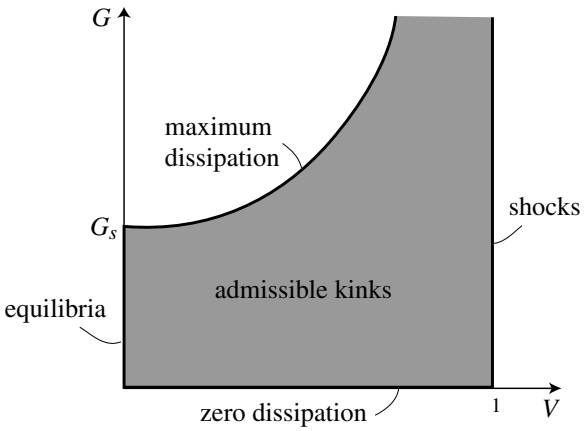

Figure 2: The admissible domain for the kinetic relations $G(V)$ for the subsonic kink solutions generated by the bilinear stress-strain law.

To find the rate of energy dissipation associated with a moving kink we need to study the traveling wave solutions of the form

$$u(x,\tau) = \hat{u}(\eta), \quad \eta = x - \tau, \tag{26}$$

subject to the conditions (18) at infinity. Substituting the traveling wave ansatz (26) in (25) and integrating once we obtain the following equation for $w = u_x = \hat{u}'(\eta)$:

$$w' = \frac{1}{VW\delta}(V^2(w_- - w) + \hat{\sigma}(w) - \hat{\sigma}(w_-)). \tag{27}$$

The states at infinity satisfy the Rankine-Hugoniot conditions automatically, because, after eliminating velocity, Eq.(22) can be written as

$$V^2(w_- - w_+) + \hat{\sigma}(w_+) - \hat{\sigma}(w_-) = 0. \tag{28}$$

Now consider the two cases $V = 0$ and $V \neq 0$ separately. In the first case, (28) reduces to $\hat{\sigma}(w_+) = \hat{\sigma}(w_-)$, and we obtain a family of piecewise constant equilibrium states inside the *trapping region*, where $V = 0$ and $|G| < G_s$. In the second case, a study of equation (27) gives the *Oleynik chord condition* (e.g. [16]). For subsonic phase boundaries, the chord condition implies that either w_+ or w_-, depending on the sign of $[\![w]\!]V$, must satisfy $\hat{\sigma}'(w) = 0$. In the case of the bilinear material considered here, the set of such configurations reduces to a single point with the critical (spinodal) strain w_c. We can therefore immediately conclude that $G_s = 1/2$.

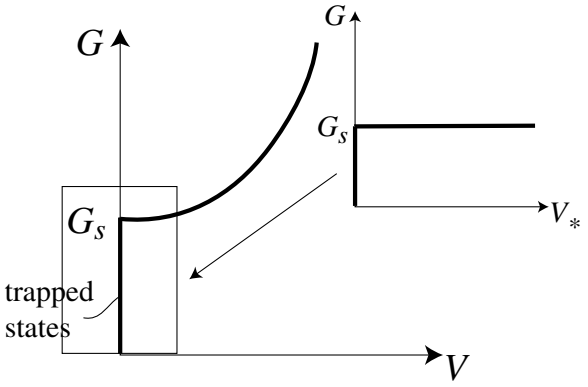

Figure 3: Kinetic relation at $V \geq 0$ resulting from the viscoelasticity model. Insert: the overdamped limit. Note that the kinetic relation for the overdamped case zooms in on the neighborhood of the depinning point.

Strain profiles. For the case of bilinear stress-strain law (21), the desired traveling wave solution with $V \neq 0$ can be written explicitly. In particular, if $V > 0$, and $w_+ < w_-$ we obtain

$$w(\eta) = \begin{cases} w_c + \dfrac{1}{1-V^2}\left(1 - \exp\left[\dfrac{(1-V^2)\eta}{VW\delta}\right]\right), & \eta \leq 0 \\ w_c, & \eta \geq 0. \end{cases} \tag{29}$$

One can see that in the limit $\delta \to 0$ (or $W \to 0$) the transition layer disappears, and the viscoelastic profile converges to the piecewise constant traveling wave of the classical elasticity problem.

Kinetic relation. Using the geometrical interpretation of the driving force G and the fact that one of the limiting strains (w_+ or w_-) must be spinodal, one can compute the area above, for $V > 0$ (or below, for $V < 0$), the graph $\hat{\sigma}(w)$ and below (above) the chord connecting the states at infinity and obtain the kinetic relation $G(V)$. According to (28), this chord, known also as Raleigh line, has the slope V^2, so that in Fig. 1 either $A_1 = 0$ ($V > 0$) or $A_2 = 0$ ($V < 0$). The kinetic relation is then given by

$$G(V) = \frac{1}{2(1-V^2)}\mathrm{sgn}(V). \tag{30}$$

As remarked above, at $V = 0$ the kinetic curve $G(V)$ contains the interval $V = 0$, $|G| < G_s$, which represents the trapped equilibrium states (see Fig. 3). The point $G_s = 1/2$ at $V = 0$ is the depinning threshold from which the solutions with $V > 0$ bifurcate (similarly, solutions with $V < 0$ bifurcate at $G = -G_s$). In addition to the trapping segment at $V = 0$

the full kinetic curve includes a $V > 0$ piece described by the Oleynik condition at nonzero V (see Fig. 3). We observe that the kinetic relation in this approximation selects exactly the upper boundary of the admissibility domain shown in Fig. 2 and therefore produces only maximally dissipative kinks. A serious deficiency of the viscoelastic approximation is that it admits only *sonic*, or Chapman-Jouget, moving discontinuities, with either w_+ or w_- taking critical (spinodal) values.

Overdamped limit. In the overdamped limit ($V \to 0$, $W \to \infty$, $V_* = VW$ finite) the sound speed c_s is infinite, and it is no longer appropriate to use it as the velocity scale. Instead we can use the rescaled velocity $V_* = VW$. Then, at $V_* > 0$ and $w_+ < w_-$ we obtain

$$w(\eta) = \begin{cases} w_c + \left(1 - \exp\left[\dfrac{\eta}{V_*\delta}\right]\right), & \eta \le 0 \\ w_c, & \eta \ge 0. \end{cases} \tag{31}$$

We reiterate that these regimes have to be supplemented by the piecewise constant trapped equilibrium states ($V_* = 0$).

The jump condition (28) reduces to $\hat{\sigma}(w_+) = \hat{\sigma}(w_-)$. The magnitude of the driving force is then constant and is given by the area enclosed between the graph $\hat{\sigma}(w)$ and the horizontal line $\hat{\sigma}(w) = \hat{\sigma}(w_+)$. The condition (28) reduces to $w_- - w_+ = 1$, so that the resulting kinetic relation is piecewise constant (see the insert in Fig. 3):

$$G(V_*) = \frac{1}{2}\mathrm{sgn}(V_*). \tag{32}$$

This piecewise constant kinetics reflects the fact that we capture only quasistatic dynamics with rate-independent dissipation [18]. One can also see that the kinetic picture in the overdamped limit can be obtained simply by zooming in on the viscoelastic kinetic law around the depinning point. Analytically this is achieved by introducing the rescaled parameter V_* which stretches the velocity coordinate around $V = 0$.

3.3 Viscosity-capillarity model

As we saw, the viscoelastic model does not admit moving subsonic discontinuities. To correct this problem, one can try to preserve in the continuum problem the effects of dispersion by expanding the energy of the discrete system (13) in Taylor series at small δ and retaining the terms up to the order of δ^2. This procedure leads to the viscosity-capillarity approximation (35), first proposed as a phenomenological model in [24, 21].

Up to the non-essential null Lagrangian, the total energy in the viscosity capillarity model can be written as

$$\mathcal{E} = \int \left[\frac{V^2 u_\tau^2}{2} + \phi(u_x) + \frac{1}{2}A^2\delta^2 u_{xx}^2\right] dx, \tag{33}$$

where

$$A^2 = \frac{1}{12}\sum_{p=1}^{q} p^4 D_p. \tag{34}$$

The model is ill-posed for $A^2 < 0$, which means that some coefficients D_p must be positive. Since $D_p = -\mu_p/E$ and $E > 0$, this implies that $\mu_p < 0$ and that the corresponding bonds are unstable.

The dynamic equations in this approximation can be written as

$$V^2 u_{\tau\tau} = (\hat{\sigma}(u_x) + WV\delta u_{x\tau} - A^2\delta^2 u_{xxx})_x. \tag{35}$$

Substituting the traveling wave ansatz (26) in (35) and integrating, we obtain the differential equation

$$A^2\delta^2 w'' + WV\delta w' + V^2 w - \hat{\sigma}(w) = V^2 w_- - \hat{\sigma}(w_-). \tag{36}$$

This equation must be considered on the infinite domain with the boundary conditions (18).

Strain profile. For the bilinear stress-strain law (21), the traveling wave solutions of (36) are given by (see [27] for more details)

$$w(\overline{\eta}) = \begin{cases} w_c + \dfrac{p_2(e^{p_1\overline{\eta}} - 1)}{(p_1 - p_2)(1 - V^2)}, & \overline{\eta} \le 0 \\ w_c + \dfrac{p_1(e^{p_2\overline{\eta}} - 1)}{(p_1 - p_2)(1 - V^2)}, & \overline{\eta} \ge 0, \end{cases} \tag{37}$$

where $\overline{\eta} = \eta/(W\delta)$ and

$$p_{1,2} = \frac{VW^2}{2A^2}\left[-1 \pm \sqrt{1 + \frac{4A^2}{W^2}\left(\frac{1}{V^2} - 1\right)}\right].$$

One can see that moving subsonic discontinuities with $w_\pm$ in the interior of the phase regions are now admissible.

Kinetic relation. The kinetic relation becomes [27]

$$G(V) = \frac{1}{2}\left(1 - V^2\right)^{-1}\left(1 + \frac{4A^2}{W^2}\left(\frac{1}{V^2} - 1\right)\right)^{-1/2}\mathrm{sgn}(V) \tag{38}$$

Observe that Eq.(38) is independent of δ, and that parameters A and W enter only through the ratio $\alpha = A/W$. Fig. 4 shows the typical kinetic curves. At finite W all

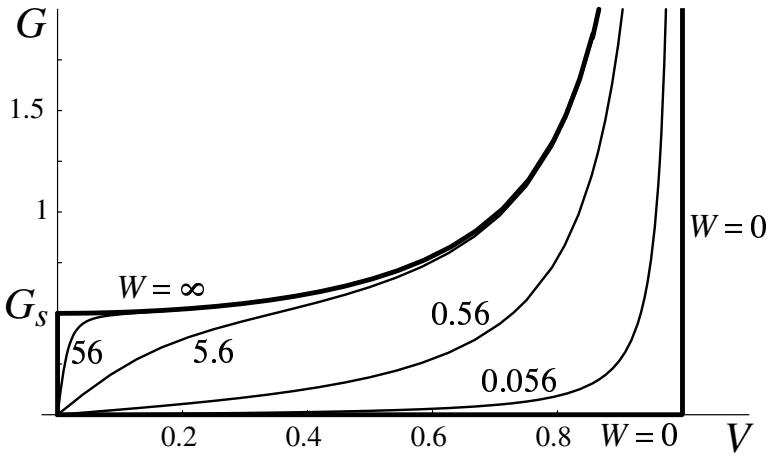

Figure 4: Kinetic relation for the viscosity-capillarity model for $V \geq 0$ at $A = 0.56$ and different values of the parameter W.

of them originate at $V = 0$ and $G(0) = 0$. This means zero depinning driving force (no lattice trapping) and contradicts the persistence of rate-independent hysteresis in quasistatic loading [20]. As W tends to infinity, the slope $G'(0)$ increases, and the curves approach the viscoelastic limit (30), which is consistent with the trapping phenomenon.

At near-sonic velocities $V \lesssim 1$ and $W > 0$ Eq. (38) converges to Eq. (30), and all kinetic curves approach the viscoelastic limit ($W = \infty$, thick upper curve). It is also important to note that in the sonic limit $V \to 1$ (and finite W) the far-field strain w_+ tends to $w_c - A^2/W^2$ and remains binodal ($w_+ < w_c$). Taking a (pointwise) limit $W \to 0$, one can see that the model predicts zero dissipation at subsonic velocities and infinite driving force at $V = 1$.

Overdamped limit. Now consider (38) at the limit $V \to 0$ and $W \to \infty$, with $V_* = VW$ remaining finite. We obtain

$$G(V) = \frac{1}{2}\left(1 + \frac{4A^2}{V_*^2}\right)^{-1/2} \operatorname{sgn}(V).$$

The resulting kinetic curves are shown in Fig. 5 for different values of A. Under the additional assumption that $A \to 0$ we obtain the viscoelastic limit.

3.4 Other quasicontinuum approximations

As we show later in the paper, in the region of its validity, the viscosity-capillarity model is sufficient to capture the dispersive features of the discrete model only in the highly

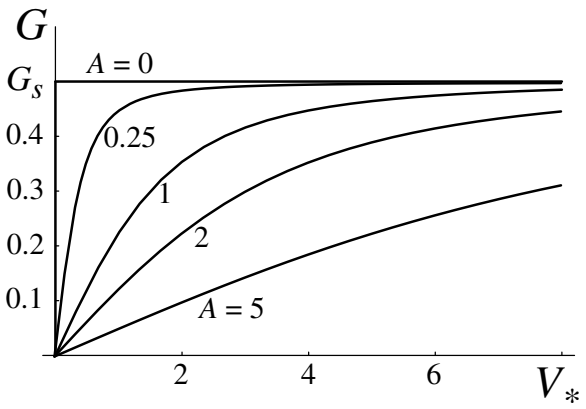

Figure 5: Kinetic relation for the viscosity-capillarity model in the overdamped limit for $V \geq 0$ at different values of the parameter A.

damped regimes. The approximation becomes progressively worse as W decreases. In particular, in the absence of internal damping ($W = 0$), the model predicts zero dissipation for subsonic phase boundaries, which completely misses the effect of radiative damping [30]. This failure of the theory suggests that in order to adequately reproduce dispersive effects in a continuum setting when the microscopic viscosity is small, other dispersive approximations of the discrete model should be considered.

For example, one can follow the approach proposed in [31] and replace the energy of the bilinear discrete system by its exact quasicontinuum analog

$$\mathcal{E}_{QC} = \int_{-\infty}^{\infty} \left[\frac{1}{2} V^2 u_\tau \mathcal{K} u_\tau + \frac{1}{2} u_x \mathcal{L} u_x - (u_x - w_c)\theta(u_x - w_c) \right] dx. \tag{39}$$

Here $\mathcal{K}$ and $\mathcal{L}$ are operators with Fourier images given by

$$\mathcal{K}(k) = \frac{(k\delta)^2}{4\sin^2(k\delta/2)}, \quad \mathcal{L}(k) = \frac{\sum_{p=1}^{q} \Psi(p) \sin^2(pk\delta/2)}{\sin^2(k\delta/2)}.$$

In this formal representation both kinetic and elastic contributions to the energy are nonlocal. Various local models can be obtained if one approximates the Fourier images of the two above operators by the first few terms in their Taylor expansions around $k = 0$. In the physical space this leads to gradient approximations of higher order for both kinetic and elastic energies, e.g.

$$\begin{aligned} \frac{1}{2} \int_{-\infty}^{\infty} u_\tau \mathcal{K} u_\tau dx \approx & \frac{1}{2} \int_{-\infty}^{\infty} \left[u_\tau^2 + \frac{1}{12} \delta^2 u_{x\tau}^2 + \frac{1}{240} \delta^4 u_{xx\tau}^2 \right] dx, \\ \frac{1}{2} \int_{-\infty}^{\infty} u_x \mathcal{L} u_x dx \approx & \frac{1}{2} \int_{-\infty}^{\infty} \left[u_x^2 + a_1 \delta^2 u_{xx}^2 + a_2 \delta^4 u_{xxx}^2 \right] dx. \end{aligned} \tag{40}$$

The coefficients a_1 and a_2 can be found from the Taylor expansion (see [31] for the exact expressions).

One can show that for sufficiently high velocities the mixed-gradient model (40) is in excellent agreement with the kinetic relations generated by the discrete model even in the Hamiltonian limit. To capture the low-velocity regime, one may have to replace the Taylor expansion around $k = 0$ by a multi-point Pade approximation which reproduces more faithfully the short-wave structure of the operators $\mathcal{K}$ and $\mathcal{L}$ (see, for instance, [4])

4 Solution of the discrete problem

In this section we return to the strongly discrete problem by assuming that $\delta = 1$. We begin by studying the general features of the solution of the discrete problem and then consider the special case $q = 2$ to focus on the detailed structure of the kinetic curves.

4.1 General features of the solution

At $\delta = 1$ Eq. (17) becomes

$$\begin{aligned} &V^2 w'' + \sum_{|p|\le q} D_p w(\eta + p) - WV(2w'(\eta) - w'(\eta + 1) - w'(\eta - 1)) \\ &= 2\theta(\eta) - \theta(\eta + 1) - \theta(\eta - 1). \end{aligned} \tag{41}$$

Using Fourier transform technique, we obtain[1] (see [30] for the details)

$$w(\eta) = \begin{cases} w_- + \displaystyle\sum_{k \in M^-(V)} \frac{4\sin^2(k/2)e^{ik\eta}}{kL_k(k,V)} & \text{for } \eta < 0 \\ w_+ - \displaystyle\sum_{k \in M^+(V)} \frac{4\sin^2(k/2)e^{ik\eta}}{kL_k(k,V)} & \text{for } \eta > 0. \end{cases} \tag{42}$$

Here the summation is over the sets $M^{\pm}(V) = \{k : L(k,V) = 0,\ \mathrm{Im} k \gtrless 0\}$, where

$$L(k,V) \equiv -4\sum_{p=1}^{q} D_p \sin^2 \frac{pk}{2} - V^2 k^2 - 4WVik \sin^2 \frac{k}{2} = 0. \tag{43}$$

The states at infinity must satisfy the jump condition

$$w_- - w_+ = \frac{1}{1 - V^2}, \tag{44}$$

[1] We assume that the moduli D_p, with $p \ge 2$, are not all zero (see [30] for the discussion of the case when this condition is not satisfied).

which coincides with the Rankine-Hugoniot condition (29). For consistency with the assumptions that led to (11) we still need to check that the formal solution is admissible in the sense that it satisfies the constraints (15).

Kinetic relation. The continuity of $w(\eta)$, together with (42) and (16) imply an additional relation between $w_\pm$ and V which can be written as either

$$w_- = w_c - \sum_{k\in M^-(V)} \frac{4\sin^2(k/2)}{kL_k(k,V)} \tag{45}$$

or

$$w_+ = w_c + \sum_{k\in M^+(V)} \frac{4\sin^2(k/2)}{kL_k(k,V)}. \tag{46}$$

Due to (44) only one of these relations is independent and is therefore furnishing the desired kinetic relation. To express this relation in a more familiar form we need to obtain the microlevel expression for the driving force. We recall that the rate of energy dissipation is

$$\mathcal{R} = V^2 W \int_{-\infty}^{\infty} (w')^2 d\eta,$$

which immediately confirms that the entropy inequality (23) is satisfied. By substituting the traveling wave solution (42) and using $\mathcal{R} = VG(V)$, we can write the expression for the driving force in the form

$$\begin{aligned} G =& VW \int_{-\infty}^{\infty} (w')^2 d\eta \\ &= 16VWi\Bigg\{ \sum_{k\in M^-(V)} \sum_{l\in M^-(V)} \frac{\sin^2(k/2)\sin^2(l/2)}{L_k(k,V)L_k(l,V)(k+l)} \\ &- \sum_{k\in M^+(V)} \sum_{l\in M^+(V)} \frac{\sin^2(k/2)\sin^2(l/2)}{L_k(k,V)L_k(l,V)(k+l)} \Bigg\}. \end{aligned} \tag{47}$$

As shown in the Appendix, this expression coincides with the formula for the driving force obtained from (24) in the continuum problem. In our bilinear case it reduces to

$$G = \frac{1}{2}(w_+ + w_-) - w_c = 2\Bigg(\sum_{k\in M^+(V)} \frac{\sin^2(k/2)}{kL_k(k,V)} - \sum_{k\in M^-(V)} \frac{\sin^2(k/2)}{kL_k(k,V)} \Bigg), \tag{48}$$

where we used (45) and (46). One can see that the driving force in both discrete and continuum cases is given by the area difference formula (24), which shows that the microscopic and macroscopic ways of assessing dissipation are consistent. Since the sets of

roots $M^{\pm}(V)$ can be computed for each V, the second equality in (48) can be viewed as a semi-analytic representation of the relation $G(V)$.

Hamiltonian limit. For $W > 0$ and $V \neq 0$ all nonzero roots of the characteristic equation have nonzero imaginary parts and are located in either upper (set $M^{+}(V)$, $\eta > 0$) or lower (set $M^{-}(V)$, $\eta < 0$) half of the complex plane. As $\eta \to \pm\infty$ the amplitude of oscillations due to the real parts of the roots tends to zero, and solution approaches the constant values $w_{\pm}$ given by (45) and (46).

As W tends to zero, some of the complex roots approach the real axis, and in the purely inertial case $W = 0$ the characteristic equation (43) becomes

$$L^0(k, V) = -4 \sum_{p=1}^{q} D_p \sin^2 \frac{pk}{2} - V^2 k^2 = 0 \tag{49}$$

This equation has a finite number of nonzero real roots responsible for the radiative damping phenomenon: short-length lattice waves emitted by the moving phase boundary carry energy away from it (see [30] for more details). These waves appear behind or ahead of the moving front, depending on whether the corresponding roots approach the real axis from the lower or upper half plane as $W \to 0$.

Indeed, let k_r be a real root of (49) and let $k_r + \kappa$ be a small complex root of (43) that approaches k_r ($\kappa \to 0$) as $W \to 0$. Expanding $L(k_r + \kappa, V) = 0$ around k_r for small κ and neglecting $O(\kappa^2)$ terms, we obtain

$$L(k_r, V) + \kappa L_k(k_r, V) = 0.$$

Recalling that $L(k, V) = L^0(k, V) - 4WVik \sin^2 \frac{k}{2}$ and $L^0(k_r, V) = 0$, we can write

$$\kappa = \frac{4WV \sin^2 \frac{k_r}{2} \left[-2WVk_r(2 \sin^2 \frac{k_r}{2} + k_r \sin k_r) + ik_r L^0_k(k_r, V) \right]}{(L^0_k(k_r, V))^2 + 4W^2V^2(2 \sin^2 \frac{k_r}{2} + k_r \sin k_r)^2}.$$

One can see that if $V > 0$, a complex root moves to real axis from above ($\mathrm{Im}\kappa > 0$) if and only if $k_r L^0_k(k_r, V) > 0$ and from below whenever $k_r L^0_k(k_r, V) < 0$. Therefore, in the limit $W = 0$ when the system becomes Hamiltonian, a particular real root contributes to the solution in front (behind) of the moving phase boundary if $k_r L^0_k(k_r, V) > 0$ (< 0). The same radiation condition was employed in [30] on the basis of the following radiation condition: the group velocity of the waves in front (behind) of the moving phase boundary must be higher (lower) than the phase boundary velocity.

We can now summarize the above analysis by specifying the sets $M^{\pm}(V)$ in (17) as they appear in the Hamiltonian limit. For $V > 0$ we obtain

$$M^{\pm}(V) = \{k : L(k, V) = 0,\ \mathrm{Im}k \gtrless 0\} \bigcup N^{\pm}(V), \tag{50}$$

where

$$N^{\pm}(V) = \{k : L(k,V) = 0,\ \mathrm{Im}k = 0,\ kL_k(k,V) \gtrless 0\} \tag{51}$$

are the sets of real roots describing radiation.

Observe now that in the Hamiltonian limit the complex roots of equation (43), which reduces to (49), appear in symmetric quadruples k, $-k$, $\overline{k}$ and $-\overline{k}$, where $\overline{k}$ denotes the complex conjugate of k. In particular, for any $k \in M^+(V) \setminus N^+(V)$ (i.e. non-real root in the upper half-plane) we have $-k \in M^-(V) \setminus N^-(V)$. Due to this symmetry and the fact that the expressions under the sums in (48) are even at $W = 0$, we can rewrite the kinetic relation in terms of the positive real roots $N_{\mathrm{pos}}(V) = \{k \in N^+(V) \cup N^-(V) : k > 0\}$ of (49). We obtain

$$G(V) = \mathrm{sgn}(V) \sum_{k \in N_{\mathrm{pos}}(V)} \frac{4\sin^2(k/2)}{|kL_k(k,V)|}. \tag{52}$$

This expression coincides, up to a dimensional rescaling, with the formula obtained in [30] by direct computation of the energy fluxes due to lattice waves moving away from a phase boundary.

Static limit. In another limiting case, $V = 0$, the continuous variable η assumes only discrete values and the strain profile becomes discontinuous at every integer η. The main advance-delay differential equation of the model reduces to a system of finite-difference equations, and we can replace the continuous Fourier transform by its discrete analog (e.g. [30]). Either using discrete Fourier transform or directly solving the difference equations, we obtain the following family of equilibrium configurations:

$$w_n(G) = \sigma_{\mathrm{M}} + \begin{cases} G + 1 + \displaystyle\sum_{k \in F^-} \frac{\sin(k/2)e^{ik(n+1/2)}}{\omega(k)\omega'(k)}, & n < 0 \\ G - \displaystyle\sum_{k \in F^+} \frac{\sin(k/2)e^{ik(n+1/2)}}{\omega(k)\omega'(k)}, & n \geq 0 \end{cases} \tag{53}$$

These lattice-trapped states are parameterized by the value of the driving force G. The parameter

$$\sigma_{\mathrm{M}} = w_c - 1/2 \tag{54}$$

is the Maxwell stress furnishing the equal area construction for the macroscopic stress-strain graph $\sigma = \hat{\sigma}(w)$. The sets $F^{\pm} = \{k : \omega^2(k) = 0, \mathrm{Im}k \gtrless 0, -\pi < \mathrm{Re}k \leq \pi\}$ contain the zeroes of the dispersion relation

$$\omega^2(k) = -4\sum_{p=1}^{q} D_p \sin^2 \frac{pk}{2}. \tag{55}$$

The admissibility requirements

$$w_n \geq w_c \quad \text{for } n \leq -1, \qquad w_n \leq w_c \quad \text{for } n \geq 0 \tag{56}$$

impose constraints on G; the set of admissible driving forces constitutes the *trapping region*. In particular, if the strain profile (53) is monotone, which occurs, for example, when all long-range interactions are repulsive ($D_p > 0$ for $p \geq 2$ [2]), the constraints (56) can be replaced by $w_0 \leq w_c$ and $w_{-1} \geq w_c$. The trapping region is then given by

$$|G| \leq G_{\mathrm{P}}, \tag{57}$$

where

$$G_{\mathrm{P}} = \frac{1}{2} + \sum_{k \in F^+} \frac{\sin(k/2) e^{ik/2}}{\omega(k)\omega'(k)} \tag{58}$$

is the *Peierls driving force* (see also [2, 28]).

The phase boundary remains trapped until the driving force reaches one of the limiting values: $G = -G_{\mathrm{P}}$, corresponding to $w_{-1} = w_c$, when the interface starts moving to the left ($V < 0$), or $G = G_{\mathrm{P}}$, corresponding to $w_0 = w_c$, when the interface starts moving to the right ($V > 0$). The two limiting equilibrium configurations represent unstable states from which the dynamic solution bifurcates. We emphasize that the Peierls driving force is generally different from the spinodal driving force $G_s = 1/2$, which describes depinning bifurcation in the viscoelastic continuum model.

Overdamped limit. Next, consider the situation when $V \to 0$ and $W \to \infty$, while their product $V_* = VW$ remains finite. Equation (44) reduces to $w_- - w_+ = 1$, which implies that the stresses $\sigma_\pm = \hat{\sigma}(w_\pm)$ in this limit are equal:

$$\sigma_+ = w_+ = w_- - 1 = \sigma_- = \sigma_{\mathrm{M}} + G.$$

This is in agreement with the jump condition (28) at $V = 0$ and we can write that $w_+ = \sigma_{\mathrm{M}} + G$ and $w_- = \sigma_{\mathrm{M}} + G + 1$. The characteristic function $L(k, V)$ in (43) can then be written as $L(k, V) = 4\sin^2(k/2)\Lambda(k, V_*)$, where $V_* = VW$ and

$$\Lambda(k, V_*) = -\sum_{p=1}^{q} D_p \frac{\sin^2(pk/2)}{\sin^2(k/2)} - V_* ik. \tag{59}$$

[2] In this case, since $D(1) < 0$, the homogeneous phases can still be stable ($\omega^2(k) > 0$ for all k) provided that the moduli responsible for long-range interactions are sufficiently small in magnitude.

The traveling wave solution (42) takes the form

$$w(\eta) = \sigma_{\rm M} + \begin{cases} G + 1 + \sum\limits_{k \in S^-(V_*)} \dfrac{e^{ik\eta}}{k\Lambda_k(k, V_*)} & \text{for } \eta < 0 \\ G - \sum\limits_{k \in S^+(V_*)} \dfrac{e^{ik\eta}}{k\Lambda_k(k, V_*)} & \text{for } \eta > 0, \end{cases} \tag{60}$$

where $S^{\pm}(V_*) = \{k : \Lambda(k, V_*) = 0,\ \mathrm{Im} k \gtrless 0\}$.

¿From (54) and condition $w(0) = w_c = \sigma_{\rm M} + 1/2$, one can see that in the overdamped limit the kinetic relation (48) reduces to

$$G = \frac{1}{2} + \sum_{k \in S^+(V_*)} \frac{1}{k\Lambda_k(k, V_*)}. \tag{61}$$

When $V_* \to \pm\infty$, the sets $S^{\pm}(V_*)$ become empty, and the driving force tends to the constant value $G(V) = (1/2)\mathrm{sgn}(V_*)$, which agrees with the behavior (32) predicted by the viscoelastic continuum model.

4.2 Case study: $q = 2$

We now focus on the special case when only nearest neighbor (NN) and next-to-nearest neighbor (NNN) interactions are taken into account. In the context of the Ising model this means standard local interaction of the "spins".

Motivated by the analogy with the Lennard-Jones type interactions [29], we assume that $-D(1) = 1 + 4D > 0$ and $D \equiv D(2) \geq 0$; the latter meaning that NNN interactions are repulsive. To facilitate the comparison with viscosity-capillarity model, we specify for the discrete NNN model the formula (34)

$$A = \sqrt{D - 1/12}. \tag{62}$$

Since $A^2 > 0$, this implies that the well-posedness of the viscosity-capillarity model requires additionally that $D > 1/12$. This means that only sufficiently strong NNN interactions can ensure stability of the viscosity-capillarity model.

Under the above assumptions the governing equations (14) reduce to

$$\begin{aligned} &V^2\ddot{w} - (1 + 4D)(w_{n+1} - 2w_n + w_{n-1}) + D(w_{n+2} - 2w_n + w_{n-2}) \\ &- WV(\dot{w}_{n+1} - 2\dot{w}_n + \dot{w}_{n-1}) = 2\theta(w_n - w_c) - \theta(w_{n+1} - w_c) - \theta(w_{n-1} - w_c). \end{aligned} \tag{63}$$

The traveling wave solution is then given by (42) with

$$L(k, V) = 4(1 + 4D)\sin^2\frac{k}{2} - 4D\sin^2 k - V^2k^2 - 4WVik\sin^2\frac{k}{2}. \tag{64}$$

Dispersion spectrum. To compute the displacement field we need to determine the roots k of the equation $L(k,V)=0$. At $V=0$ this equation has real roots $k=2\pi n$, for any integer n; if $D>0$ there are also complex roots

$$k = 2\pi n \pm i\lambda, \tag{65}$$

where

$$\lambda = \operatorname{arccosh}\left(\frac{1}{2D}+1\right). \tag{66}$$

Notice that λ tends to infinity as $D\to 0$, and therefore at $D=0$ the complex roots disappear. For $V>0$ the roots can be computed via an iterative numerical procedure which uses the known roots at $V=0$ as initial guesses. The general configuration of nonzero roots can be understood from Fig. 6, where due to the symmetry of the problem only roots with positive real part had to be shown.

In summary, there are two types of roots and they are shown in Fig. 6 as solid black and grey branches parameterized by the velocity V. The black branches emanate from the real roots $k=2\pi n$ corresponding to $V=0$; for small enough W, they can also bifurcate from the branch of purely imaginary roots. These branches contribute to the oscillatory behavior of the solution and create the dynamic structure of the core that disappears at $V=0$. The grey branches emanate from (65). With the exception of the branch originating at $k=-i\lambda$ and $V=0$ (along which the roots tend to zero as V increases), the grey branches exist only at $D>0$ and are responsible for the core structure that is inherited from statics. As W tends to zero, the black branches move closer to each other (see Fig. 6b). In the purely inertial limit ($W=0$, [30]) these branches get attached to each other in such a way that some of the roots become real. For contrast, they are shown in Fig. 6a by a thinner line from which the complex roots (black curves) bifurcate.

As W becomes larger, each black branch folds, and in the overdamped limit they become straight lines $k=2\pi n$ (see Fig. 6c). The limiting roots (the zeroes of $\sin^2(k/2)$) are no longer singularities and hence do not contribute to the solution. To see this, we recall that $L(k,V)=4\sin^2(k/2)\Lambda(k,V_*)$, so that $4\sin^2(k/2)$ appears in both numerator and denominator. The relevant nonzero roots are those of $\Lambda(k,V_*)=0$, with

$$\Lambda(k,V) = 1 + 4D\sin^2\frac{k}{2} - V_* ik. \tag{67}$$

Therefore, as we see in Fig. 6d, only grey branches survive in the overdamped limit.

As D tends to zero, all grey branches except the one coming out of $k=-i\lambda$, $V=0$, move to infinity. Thus at $D=0$ (NN model) only this and the black branches (at finite W) remain. In the overdamped limit the only nonzero root of $\Lambda(k,V_*)=0$ at each V_* (the single surviving grey branch) is given by $k=-i/V_*$. As a result, the strain profile (60) in this case coincides with its continuum counterpart (31).

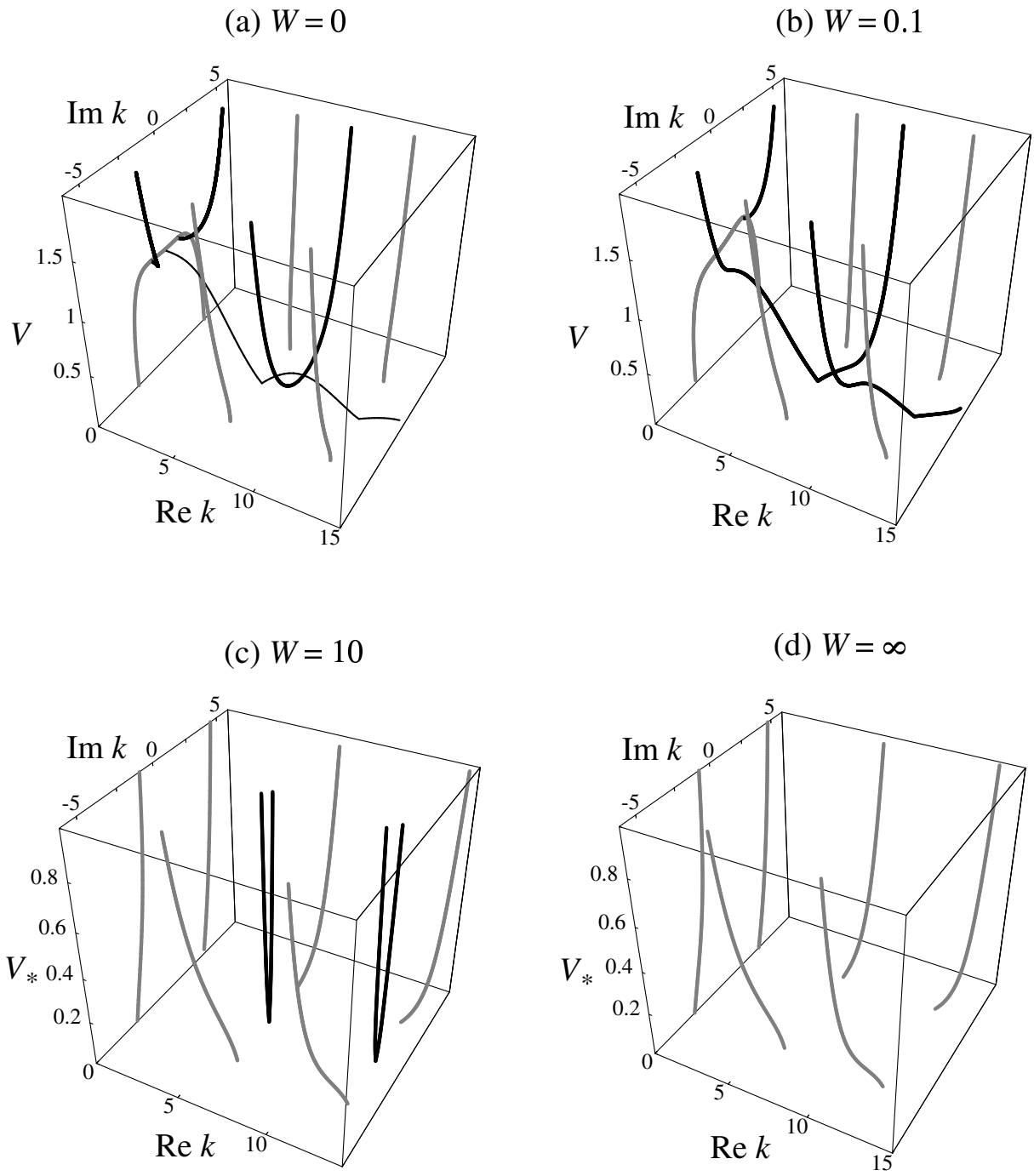

Figure 6: The structure of nonzero roots of $L(k, V) = 0$ (a, b and c) and $\Lambda(k, V_*)$ (d) at different W. In all pictures $D = 1/16$. In (c) and (d) $V_* = VW$ is plotted along the vertical axis.

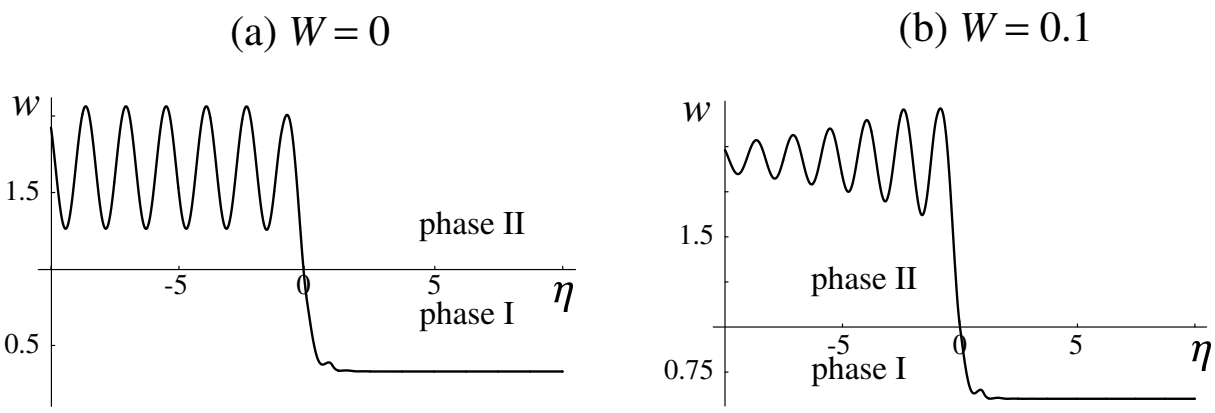

Figure 7: Strain profiles for traveling wave solutions with $V = 0.5$: (a) $W = 0$; (b) $W = 0.1$. Here $D = 1/16$ and $w_c = 1$.

Strain profiles. Typical strain profiles of the traveling wave solutions (42) with sufficiently large velocity ($V = 0.5$) are shown Fig. 7 where the Hamiltonian case ($W = 0$) is compared with the case of nonzero viscosity ($W = 0.1$). One can see that solutions of the discrete problem exhibit lattice scale oscillations (that become damped at $W > 0$), while neither classical elasticity nor viscoelastic or viscosity-capillarity models predict any oscillatory behavior of the displacement fields.

Admissibility. As we have already mentioned, some of the solutions formally constructed using (42), may have to be discarded if they violate the constraints (15). For instance, in both cases shown in Fig. 8 ($V = 0.25$ and $V = 0.1$) the oscillating strain at small $\eta > 0$ is in phase II, when the single interphase ansatz requires it to be in phase II. In fact, a systematic numerical study reveals several small-velocity intervals (velocity gaps) where the formal traveling wave solutions are not admissible; in these intervals of velocity a more complex dynamics is expected to take place. These prohibited intervals become smaller at larger D, for example, Fig. 9 shows that at $D = 0.4$ the solution with $V = 0.25$, which was discarded at $D = 1/16$, becomes admissible. This takes place due to the regularizing role of D: as D increases, the grey branches of the characteristic equation move closer to the real axis which make the transition layer wider and suppress the oscillations near the phase boundary. The same effect can be achieved by increasing W.

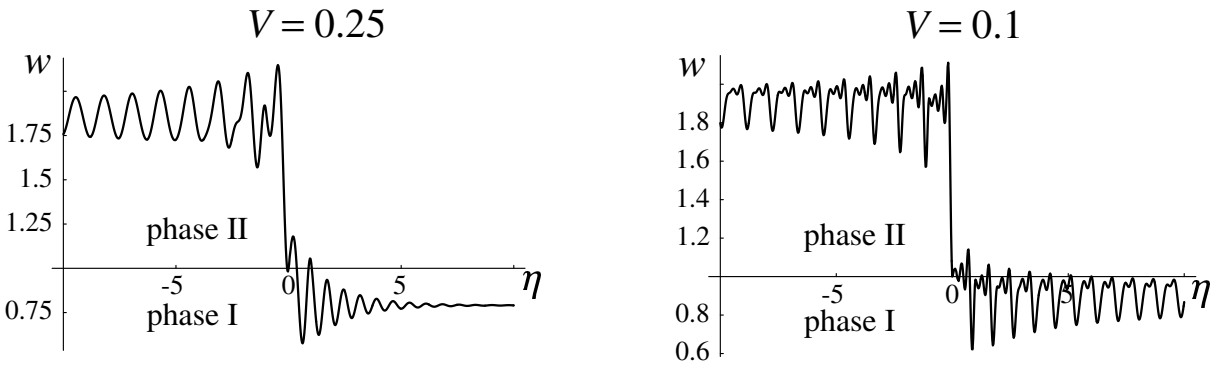

Figure 8: Examples of inadmissible solutions at $D = 1/16$, $W = 0.1$ and $w_c = 1$: (a) $V = 0.25$; (b) $V = 0.1$. Solutions violate the constraints (15) and hence are not admissible.

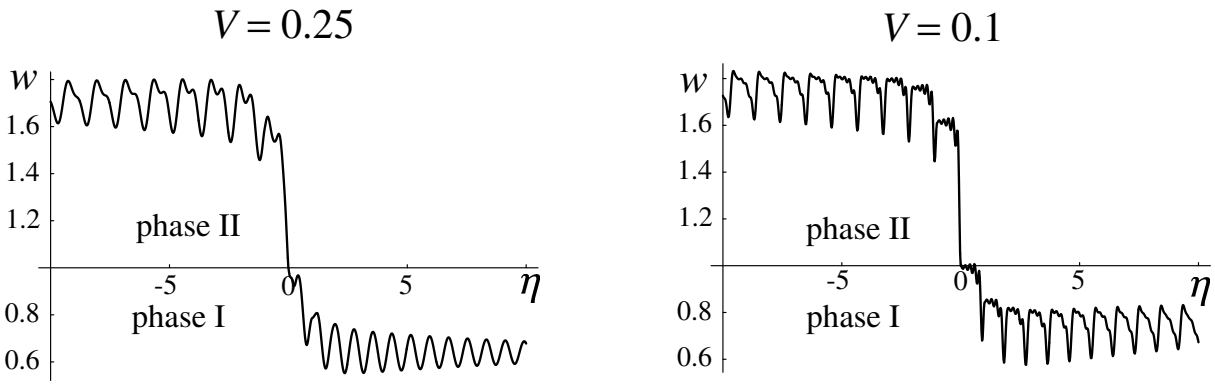

Figure 9: Strain profiles at $D = 0.4$, $W = 0.1$ and $w_c = 1$. Solution at $V = 0.25$ is now admissible but solution at $V = 0.1$ still violates (15).

Static limit. Single-interface equilibria (53) with phase boundary located at $n = m$ can be presented in the form [6, 7, 28]

$$w_n^m(G) = \sigma_{\rm M} + \begin{cases} G + 1 - \dfrac{\exp(\lambda(n-m-1/2))}{2\cosh(\lambda/2)}, & n < m \\ G + \dfrac{\exp(-\lambda(n-m-1/2))}{2\cosh(\lambda/2)}, & n \geq m, \end{cases} \tag{68}$$

where λ is given by (66). These solutions exist for G in the trapping region (57), with the Peierls driving force given by

$$G_{\rm P} = \frac{1}{2\sqrt{1+4D}}. \tag{69}$$

Note that the Peierls force is nonzero and $G_{\rm P} < G_s$ for all finite $D > 0$; at $D = 0$ we have $G_{\rm P} = G_s$.

A subtle but important feature distinguishing our model from the Frenkel-Kontorova (FK) model is that D does not depend on δ and the Peierls force remains finite in the continuum limit $\delta \to 0$. In contrast, in the FK model the Peierls force is proportional to δ and thus disappears in the continuum limit (e.g [10]).

Overdamped limit. In the overdamped limit ($V \to 0$, $W \to \infty$, $V_* = VW$ finite) the equation (63) can be "integrated" to yield

$$V_* \dot{w}_n = D(w_{n+1} - 2w_n + w_{n-1}) - \hat{\sigma}(w_n) + \sigma, \tag{70}$$

where $\sigma = \sigma_{\rm M} + G$ is the applied stress. Equation (70) coincides with the discrete reaction-diffusion equation, which is also known as Nagumo system in biology [6, 8] or the overdamped FK system in dislocation dynamics [3, 10]. We emphasize that the equivalence between our and FK models can be established only in the overdamped and statics limits: when the inertia term in (63) is nonzero, the two models yield different dynamics [30]. Observe also that at $D = 0$ the equation (70) coincides with the analogous equation obtained in continuum viscoelastic model in overdamped limit.

The traveling wave solution in the overdamped limit is given by (60) with $\Lambda(k, V)$ taken from (67). As $V \to 0+$ the strain profile approaches the staircase shown in Fig. 10 ($V_* = 0+$); at larger V_*, the staircase structure smoothens out. The corresponding "stick-slip" evolution of $w_n(t)$ at small V_* for $n = 0, 1, 2$ can be reconstructed from Fig. 11.

Notice that the small-V_* solutions can be viewed as singular perturbations of $w^{V_*=0+}(\eta)$, in particular, they replace steps by thin transition layers with the width proportional to

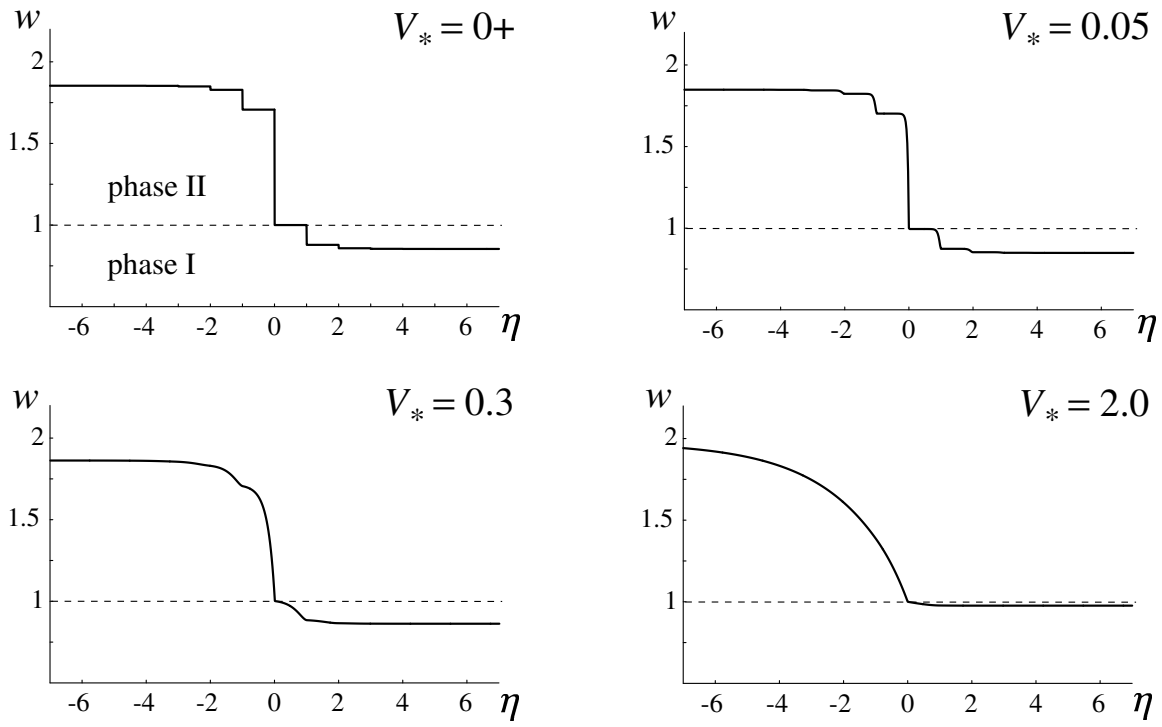

Figure 10: Strain profiles in the overdamped limit at $D = 1/4$, $w_c = 1$.

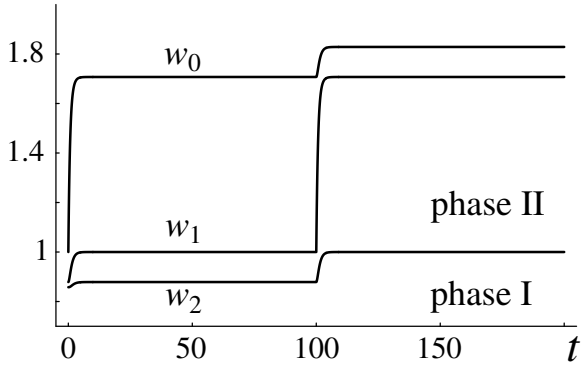

Figure 11: Evolution of strain in the zeroth, first and second springs at small V in the overdamped limit. Parameters: $V_* = 0.01$, $D = 1/4$, $w_c = 1$.

V_* (e.g. [6]). During the time period $T = 1/V_*$ the dynamics can be interpreted as an approach toward the closest "virtual attractor" given by a stable equilibrium at $G = G_{\rm P} - 0$, just below the boundary of the trapping region. For instance, if initially the phase boundary is at $n = 0$ ($w_0(0) = w_c$), and if G is just above the trapping region, the closest virtual attractor is s_n^0 where $s_1^0 = w_c - 0$, and $s_n^m \equiv w_n^m(G_{\rm P} - 0)$. The attractor is only virtual because at $G > G_{\rm P}$ no equilibrium solutions actually exist, and, as a result, it is never attained. Thus, as soon as $w_1(t)$ reaches w_c, the whole process starts again, with solution "attracted" by s_n^1 and so on.

5 Comparison of discrete and continuum models

In this section we first review the specific structure of the kinetic relation emerging in our NNN model, and then use it as a benchmark for comparison of the discrete model with its continuum approximations.

In the Hamiltonian limit ($W = 0$) the kinetic relation in the discrete NNN model reduces to (52), with the driving force fully determined by the real roots of the dispersion relation. In this case there is an infinite number of resonance velocities V_i corresponding to real k satisfying equations $L(k, V_i) = 0$ and $L_k(k, V_i) = 0$ simultaneously. At such velocities, the driving force diverges which creates singular peaks on the kinetic curves (see Fig. 12a). At nonzero W the resonances are replaced by oscillations; the amplitude of oscillations decreases as W increases (Fig. 12b,c). The shaded regions in Fig. 12 correspond to non-admissible traveling waves that must be removed. As W increases, the velocity gaps become more narrow. The effect of D can be seen from the comparison of Fig. 13 ($D = 0.4$) and Fig. 12b ($D = 1/16$): at larger D one inadmissibility interval may transform into several ones.

We can now move to the comparison of the discrete and continuum models. Fig. 14 shows discrete kinetic relations corresponding to a fixed $D = 0.4$ and different W. This value of D is equivalent to $A = 0.56$ in the viscosity-capillarity model (recall (62)), and Fig. 14 should be juxtaposed against Fig. 4. Although the overall behavior of the kinetic curves in the discrete theory and in viscosity capillarity model is similar, the discrete kinetics has two distinct features. First, due to the nonzero value of the Peierls force and the non-existence of traveling wave solutions at small V, there is a region in the left bottom corner of the discrete diagram (below the schematic dashed line), where there are no admissible kinetic curves. In contrast, in continuum viscosity-capillarity model all curves start from $V = 0$ and therefore the left bottom corner is filled in. Second, the discrete model predicts nonzero dissipation in the Hamiltonian limit ($W = 0$), which results in the presence of a lower boundary below which there are no kinetic curves. Meanwhile, kinetic curves in the viscosity-capillarity model can exist anywhere inside the

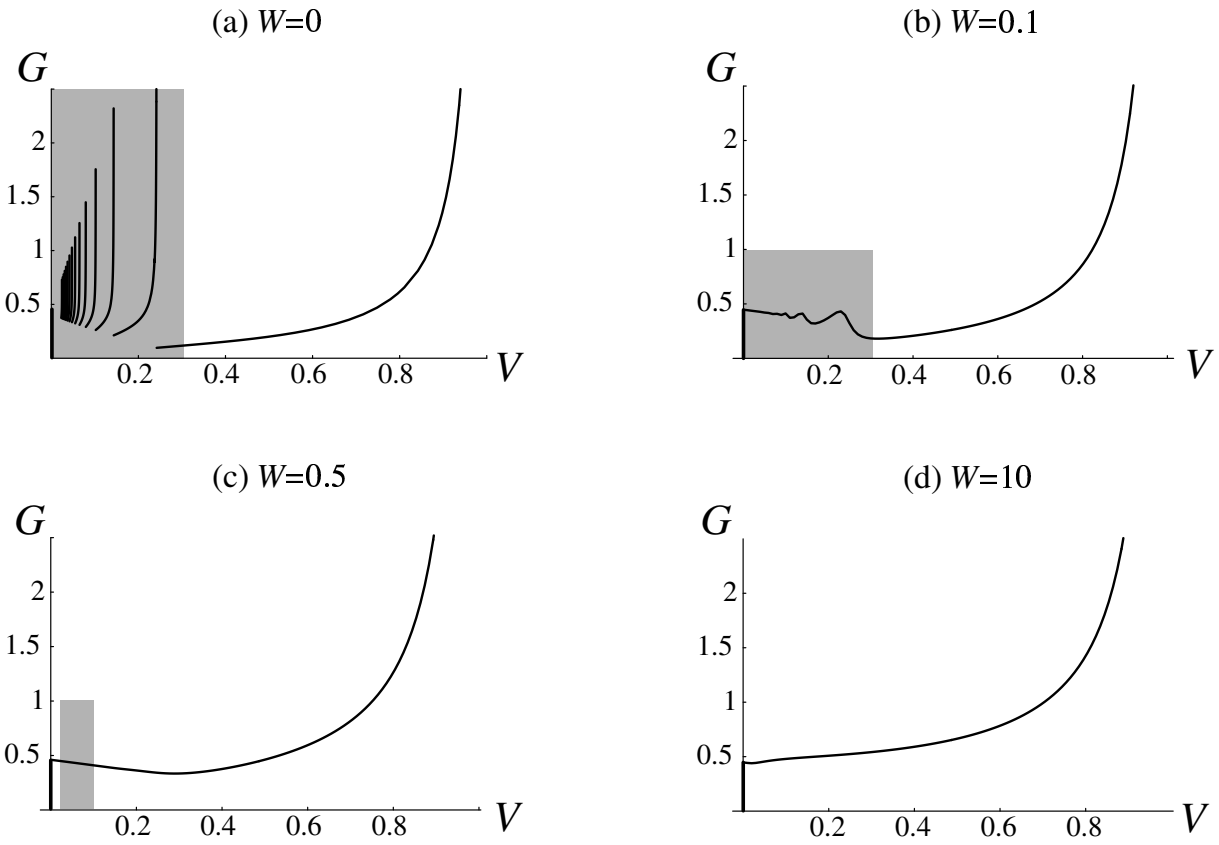

Figure 12: Kinetic relations $G(V)$ at different W. Here $D = 1/16$. The shaded regions indicate the portions of the graphs that should be removed because the corresponding traveling wave solutions violate the admissibility conditions (15).

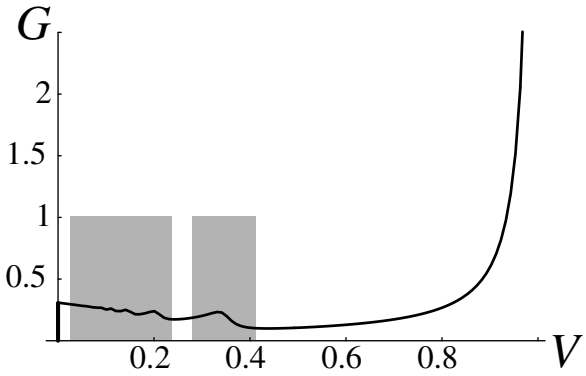

Figure 13: Kinetic relation $G(V)$ at larger D. Here $D = 0.4$ and $W = 0.1$. This figure can be compared to Fig. 12b.

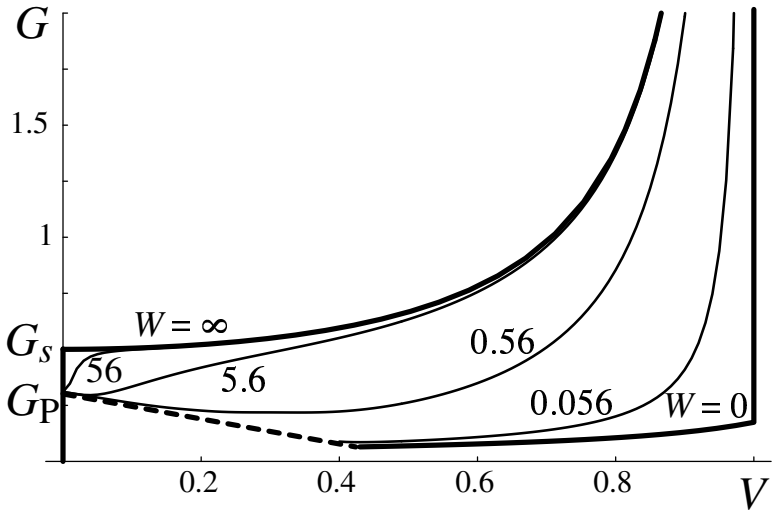

Figure 14: Kinetic relation for discrete model at different W. Here $D = 0.4$, which corresponds to $A = 0.56$ in the viscosity-capillarity model, the case depicted in Fig. 4. The portions of the small-W curves that contain non-admissible solutions have been removed. The solid dashed line is the (schematic) boundary of the region in the left bottom corner where there are no admissible traveling wave solutions.

bounds predicted by the classical continuum theory (see our Fig. 2).

As the phase boundary velocity approaches the sonic limit ($V \to 1$) the behavior of the kinetic curves starts to exhibit universality.

It will be convenient to first look at the Hamiltonian limit $W = 0$. Recall that in this case the driving force (52) is determined entirely by the positive real roots of $L(k, V) = 0$ and when $V \lesssim 1$, there is only one positive real root. Expanding the dispersion relation at small k and $W = 0$, we obtain

$$V^2 \approx 1 + \left(D - \frac{1}{12}\right)k^2 - \frac{1}{6}\left(D - \frac{1}{60}\right)k^4.$$

This means that for weak NNN interactions ($D < 1/12$), the relevant root approaches zero as $V \to 1-$. Substituting the above approximation into the expansion of (52) near small k, we obtain

$$G \approx \frac{1}{2(1 - V^2)}. \tag{71}$$

One can see that this asymptotics at $V \to 1-$ coincides with (30) (see also Fig. 12a, where $D = 1/16$). Meanwhile, for stronger NNN interactions ($D > 1/12$, the interval where viscosity-capillarity model is valid), the single positive root approaches a nonzero value k_s as $V \to 1-$, and this leads to a finite value of the driving force [30]. At $V = 1+$ the driving force becomes infinite, due to the addition of a root at zero. We can then conclude that the resulting kinetic relation has a "corner" at $V = 1$ (see, for example, the curve $W = 0$ in Fig. 14, where $D = 0.4$).

If now $W > 0$, the sum of residues over the set $M^+(V)$ tends in the sonic limit to a finite value $s > 0$, which increases as $W \to 0$ and tends to zero as $W \to \infty$. Thus $w_+ \to w_c - s$ (recall (46)), while $w_- \to w_c - s + 1/(1 - V^2)$ (recall (44)). Hence (48) yields the asymptotics (71) for $V \lesssim 1$, regardless of the value of D. The width of the boundary layer where this asymptotic is valid increases with W (see the $W > 0$ curves in Fig. 14). The asymptotic behavior of the kinetic curves at $W > 0$ is thus the same as in the viscosity-capillarity and viscoelasticity model.

In the overdamped limit the graphs showing the kinetic relations at different D are presented in Fig. 15. When $D = 0$ (no NNN interactions) the set S^+ is empty, and the driving force (61) is constant: $G = G_s = 1/2$. We recall that in this case the discrete equation (70) coincides with the continuum equation. At $D > 0$ the driving force approaches the Peierls value from above as V_* tends to zero and $G(0+) = G_{\mathrm{P}}$. At large V_*, solution approaches the one for $D = 0$, so that G tends to G_s. In Fig. 15, which should be compared to Fig. 5, one can see the blow up of the domain in the parameter space where V is small and W is large. Both figures show a similar approach to the constant value of the driving force at $V_* > 0$ as the nonlocality parameter (D or A) decreases. At the same time, while the viscosity-capillarity model always sets Peierls force at zero

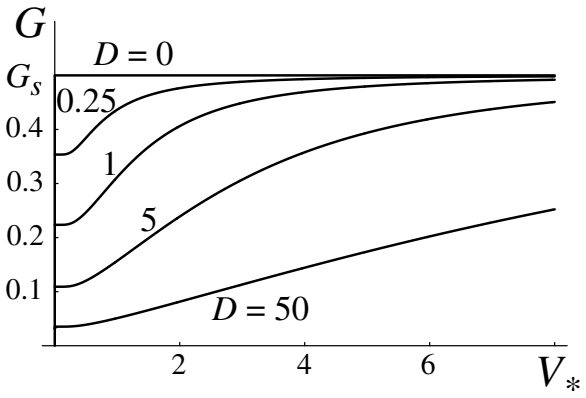

Figure 15: Kinetic relations at different D in the overdamped limit.

and yields piecewise constant dynamics in the limit when $A = 0$, the Peierls force in the discrete model is always nonzero (recall that $D = 1/12$ in this limit).

To see more clearly how the discrete theory is approximated by its formal continuum limits, it is instructive to consider the discrete model at the intermediate values of δ. In particular, we expect to see that in the limit $\delta << 1$ (weakly discrete limit) the predictions of the discrete model are comparable with those of viscosity-capillarity and viscoelasticity models everywhere outside thin boundary layers in the space of parameters. The persistence of the boundary layers is expected due to the singular nature of the perturbation associated with the parameter δ.

For the general $\delta \neq 0$ the solution of the equation (17) is given by

$$w(\eta) = \begin{cases} w_- + \displaystyle\sum_{k \in M^-(V)} \frac{4\sin^2(k/2)e^{ik\eta/\delta}}{kL_k(k,V)} & \text{for } \eta < 0 \\ w_+ - \displaystyle\sum_{k \in M^+(V)} \frac{4\sin^2(k/2)e^{ik\eta/\delta}}{kL_k(k,V)} & \text{for } \eta > 0. \end{cases} \tag{72}$$

The driving force is still (48), where the summations are over the roots of $L(k,V)$ from (43). Interestingly, the value of the Peierls driving force is independent of δ.

We begin by comparing the strain profiles generated by the weakly discrete model (72) to those obtained using viscoelasticity and viscosity-capillarity models. Recall that A is related to D through (62) and that viscosity-capillarity approximation is only meaningful in the strongly nonlocal regime $D > 1/12$. Fig. 16 compares the strain profiles generated by discrete (solid curves), viscoelasticity (dashed curves) and viscosity-capillarity (dotted curves) models at $D = 0.4$, $\delta = 0.01$ and $W = 1$. One can see that at higher velocities the strain profiles generated by the discrete and viscosity-capillarity models become closer.

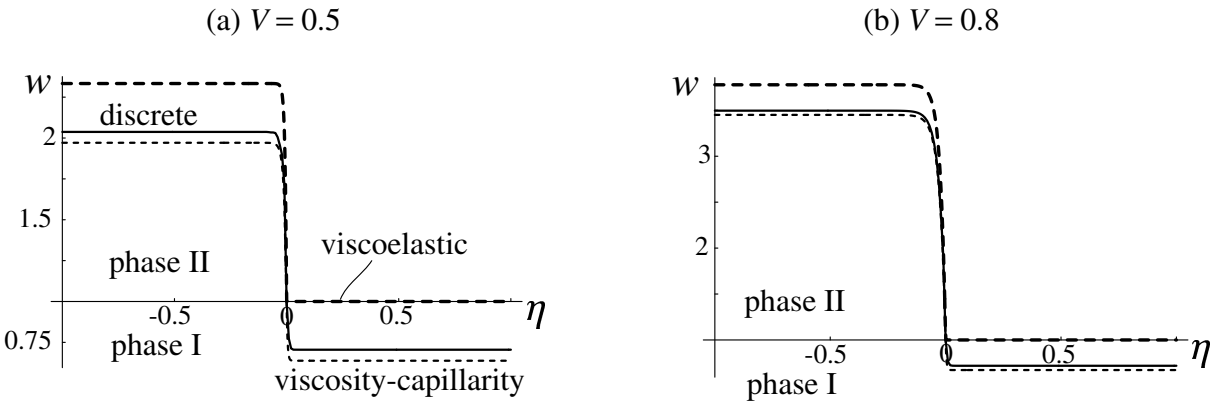

Figure 16: Strain profiles generated by the discrete (solid curves), viscoelasticity (dashed curves) and viscosity-capillarity (dotted curves) models at (a) $V = 0.5$ and (b) $V = 0.8$. Here $D = 0.4$, $W = 1$, $\delta = 0.01$ and $w_c = 1$.

This is expected since at higher V the effective viscosity is higher, and the dissipation due to viscosity plays a larger role, making the flaws in the approximation of dispersion less visible. Note, however, that strain profiles in both discrete and viscosity-capillarity cases predict w_+ below the spinodal value w_c, while the viscoelastic model gives $w_+ = w_c$. As W tends to infinity, w_+ tends to the critical value in all three models.

Fig. 17 compares the kinetic curves in different models at $W = 0.1$, 1 and 10 for $D = 0.4$. One can see that the kinetic curves for the discrete model (solid curves) start at the Peierls value $G(0+) = G_{\rm P}$, which is less than spinodal value $G_s = 1/2$ for $D > 0$ (here $G_{\rm P} = 0.31$), and approach the viscosity-capillarity (dotted curves) and viscoelastic continuum (dashed) curves at larger velocities. While the viscosity-capillarity model underestimates the driving force at small velocities, since it requires $G(0) = 0$, the viscoelastic model overestimates it, since it starts at $G(0+) = G_s$. At sufficiently large V, all three curves display the same asymptotic behavior given by (30). How "fast" this asymptotics is approached depends on W. At higher values of W, the width of the small-velocity boundary layer where discrete model behaves differently from its continuum and quasicontinuum counterparts diminishes. On the other hand, the range of velocities where discrete and viscosity-capillarity models predict different behaviors increases as W tends to zero. In the limiting case, $W = 0$, the viscosity-capillarity model incorrectly predicts that $G \equiv 0$ for $V < 1$, while the discrete model always requires a nonzero driving force for the phase boundary to move(see Fig. 12a). Despite this shortcoming, the viscosity capillarity model still provides a valid lower bound for the driving force.

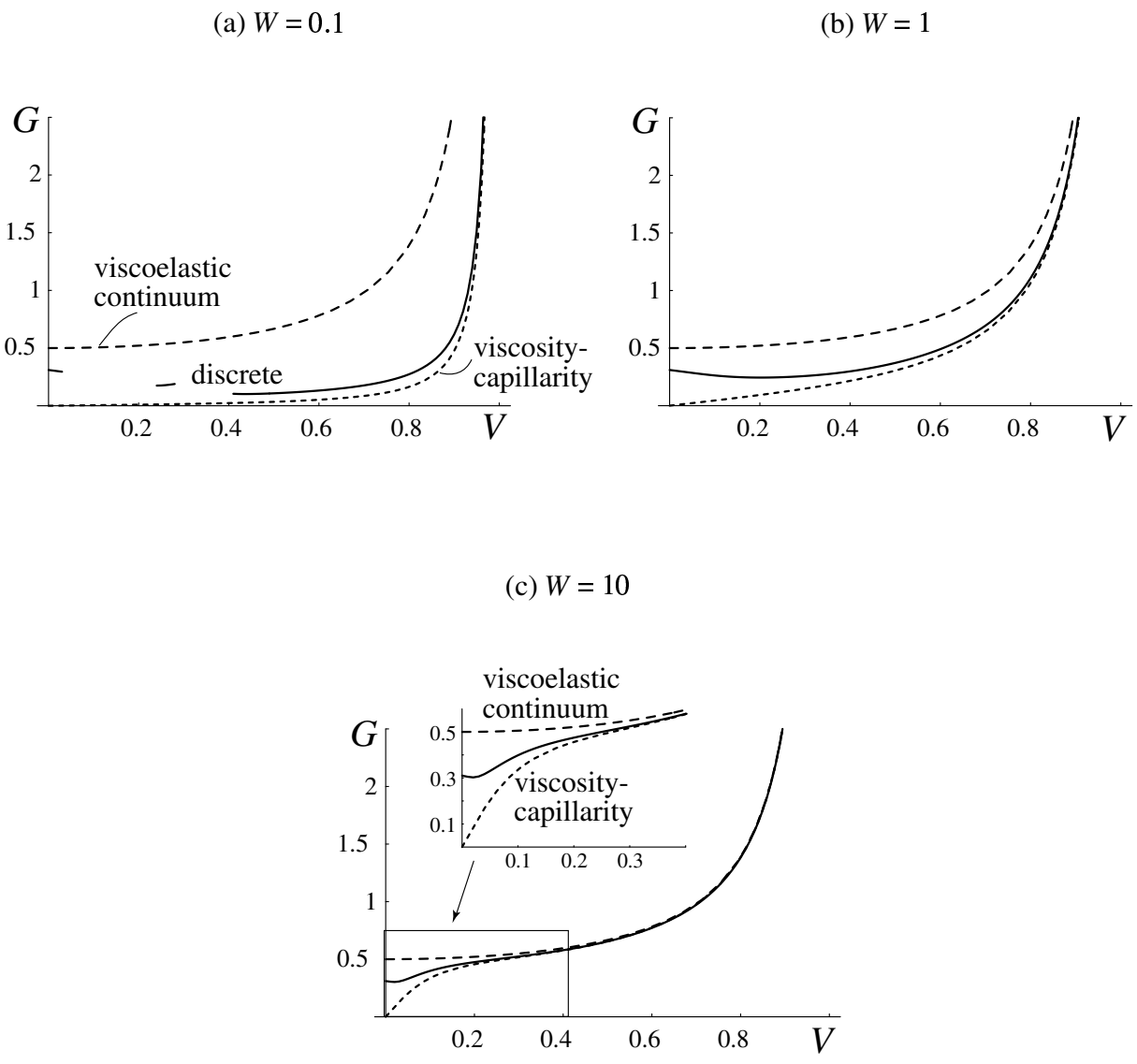

Figure 17: Kinetic relations generated by the discrete model (solid curves) and viscosity capillarity approximation (dotted curves) at (a) $W = 0.1$, (b) $W = 1$ and (b) $W = 10$. Here $D = 0.4$. In (a) portions of the discrete kinetic relation that contain inadmissible solutions have been removed. The kinetic curve generated by viscoelastic continuum model (dashed curve), independent of W, is also shown for comparison.

6 Concluding remarks

In this paper we considered the simplest discrete dynamical model of a prototypical martensitic phase transition, amenable to detailed analytical study. We focused on the interplay between three main physical mechanisms responsible for the specificity of the dynamics of martensitic phase boundaries, namely, *dispersion*, *dissipation*, and *inertia*. We introduced three nondimensional measures of the corresponding effects: δ, W, and V. Despite its simplicity, the model also allows for *nonlocality* which in the simplest can be characterized by one additional nondimensional parameter D. The main challenge was to distinguish qualitatively different kinetic regimes in the space of parameters δ, W, V and D.

A more specific problem addressed in this paper was to what extent the discrete model can be replaced in the domain $\delta \sim 0$ by its quasicontinuum approximation. Having a fully analytical benchmark, we could test three continuum candidates broadly employed in the modeling of martensitic phase transitions: elasticity, viscoelasticity and viscosity-capillarity models. We have temporarily left aside some other more sophisticated quasi-continuum options.

After showing that the naive continuum limit $\delta \to 0$, corresponding to classical elasticity theory, fails to provide the necessary information regarding the kinetics of phase boundaries, we have focused on two other continuum approximations of the discrete model - viscoelasticity, a local continuum model which includes only dissipation, and viscosity-capillarity, a weakly nonlocal quasicontinuum model that incorporates both dispersion and dissipation. We systematically compared the kinetic relations and traveling wave profiles resulting from these two models with the one taken from the explicit solution of the discrete problem.

Based on this analysis, we can make the following conclusions:

1. The defining feature of the discrete model is lattice trapping. In the presence of nonlocality ($D > 0$) the value of the Peierls force in the discrete model is below the spinodal limit and remains nonzero for all finite D. In contrast, the viscosity-capillarity model predicts identically zero Peierls force. At large W, the lattice trapping is mimicked in the viscosity-capillarity model by a rapid increase of the driving force with velocity around $V = 0$. Even though the viscoelasticity model captures the trapping phenomenon qualitatively, it overestimates the value of the Peierls force by equating it to the spinodal force.

2. If stable, all three models predict the same asymptotics for the kinetic relation in the regime of $|V| \lesssim 1$, where inertial effects dominate.

3. The overdamped limit represents a blow up of the kinetic curves in the region of large W and small V, where inertial effects can be neglected. In the absence of

nonlocality ($D = 0$ in the discrete case and $D = 1/12$ in case of viscosity-capillarity model) all three models behave similarly. In the presence of nonlocality the behavior of the three models around $V = 0$ is qualitatively different.

4. The most sophisticated among our quasicontinuum approximations, the viscosity-capillarity model, becomes progressively less adequate as W decreases. In particular, the viscosity-capillarity model predicts zero dissipation at $W = 0$ in the subsonic regime while the discrete theory always remains macroscopically dissipative due to the phenomenon of radiative damping. The viscosity-capillarity model also can not be used in the weakly nonlocal regime with $D < 1/12$ where it is unstable. To deal with the regimes where viscosity-capillarity model fails, alternative quasicontinuum models should be constructed and we refer to [31, 4] for the realistic propositions.

Acknowledgements. This work was supported by the National Science Foundation grant DMS-0443928 (A.V.).

Appendix

In this appendix we prove that the formulas (47) and (48) for kinetic relation are equivalent. We start by considering the double sums in (47). For convenience, we denote the summand by

$$f(k,l) = \frac{\sin^2(k/2)\sin^2(l/2)}{L_k(k,V)L_k(l,V)(k+l)}.$$

and omit the explicit reference to dependence on V. Now observe that

$$\sum_{k\in M^-}\sum_{l\in M^-} f(k,l) = \sum_{k\in M^-}\sum_{l\in M} f(k,l) - \sum_{k\in M^-}\sum_{l\in M^+} f(k,l)$$

and

$$\sum_{k\in M^+}\sum_{l\in M^+} f(k,l) = \sum_{k\in M^+}\sum_{l\in M} f(k,l) - \sum_{k\in M^+}\sum_{l\in M^-} f(k,l).$$

Here $M = M^+ \cup M^-$. Since $f(k,l) = f(l,k)$, the mixed sums can be interchanged, and thus

$$\sum_{k\in M^-}\sum_{l\in M^-} f(k,l) - \sum_{k\in M^+}\sum_{l\in M^+} f(k,l) = \sum_{k\in M^-}\sum_{l\in M} f(k,l) - \sum_{k\in M^+}\sum_{l\in M} f(k,l).$$

Now, using Residue Theorem, we can write

$$\lim_{R\to\infty} \frac{1}{2\pi i}\oint_{|l|=R} \frac{\sin^2(l/2)dl}{(k+l)L(l,V)} = \sum_{l\in M} \frac{\sin^2(l/2)}{(k+l)L_k(l,V)} + \frac{\sin^2(k/2)}{L(-k,V)}.$$

But the integral in the left hand side vanishes as the radius R of the circular contour tends to infinity, and thus we have

$$\sum_{l\in M} \frac{\sin^2(l/2)}{(k+l)L_k(l,V)} = -\frac{\sin^2(k/2)}{L(-k,V)}.$$

Recalling that $k \in M$ satisfy the equation (43), we have

$$L(-k,V) = L(k,V) + 8WVik\sin^2\frac{k}{2} = 8WVik\sin^2\frac{k}{2}.$$

Thus,

$$\sum_{l\in M} \frac{\sin^2(l/2)}{(k+l)L_k(l,V)} = -\frac{1}{8WVik}.$$

and we obtain

$$\begin{aligned} &8WVi\Big(\sum_{k\in M^-}\sum_{l\in M^-} f(k,l) - \sum_{k\in M^+}\sum_{l\in M^+} f(k,l)\Big) \\ &= \sum_{k\in M^+} \frac{\sin^2(k/2)}{kL_k(k,V)} - \sum_{k\in M^-} \frac{\sin^2(k/2)}{kL_k(k,V)}, \end{aligned}$$

which shows that (47) and (48) are equivalent, as claimed.

References

[1] R. Abeyaratne and J.K. Knowles. Implications of viscosity and strain gradient effects for kinetics of propagating phase boundaries in solids. *SIAM Journal of Applied Mathematics*, 51:1205–1221, 1991.

[2] O. M. Braun, Yu. S. Kivshar, and I. I. Zelenskaya. Kinks in the Frenkel-Kontorova model with long-range interparticle interactions. *Physical Review B*, 41:7118–7138, 1990.

[3] A. Carpio and L. L. Bonilla. Depinning transitions in discrete reaction-diffusion equations. *SIAM Journal of Applied Mathematics*, 63(3):1056–1082, 2003.

[4] M. Charlotte and L. Truskinovsky. Towards multi-scale continuum elasticity theory. *Cont. Mech. Thermodyn.*, 2007.

[5] H. Fan and M. Slemrod. Dynamic flows with liquid/vapor phase transitions. In D. Serre S. Friedlander, editor, *Handbook of mathematical fluid dynamics*, volume 1, pages 373–420. Elsevier, 2002.

[6] G. Fáth. Propagation failure of traveling waves in discrete bistable medium. *Physica D*, 116:176–190, 1998.

[7] R. Hobart. Peierls stress dependence on dislocation width. *J. Appl. Phys.*, 36(6), 1965.

[8] J. P. Keener. Propagation and its failure in coupled systems of discrete excitable cells. *SIAM Journal of Applied Mathematics*, 47(3):556–572, 1987.

[9] P. G. Kevrekidis, I. G. Kevrekidis, A. R. Bishop, and E. S. Titi. Continuum approach to discreteness. *Physical Review E*, 65:046613, 2002.

[10] O. Kresse and L. Truskinovsky. Mobility of lattice defects: discrete and continuum approaches. *Journal of the Mechanics and Physics of Solids*, 51:1305–1332, 2003.

[11] R.V. Krishnan. Stress induced martensitic transformations. *Mater. Sci. Forum*, 3:387–398, 1985.

[12] P. G. LeFloch. *Hyperbolic systems of conservation laws.* ETH Lecture Note Series. Birkhouser, 2002.

[13] T. Lookman, S. R. Shenoy, K. O. Rasmussen, A. Saxena, and A. R. Bishop. Ferroelastic dynamics and strain compatibility. *Physical Review B*, 67(2):024114, 2003.

[14] G. B. Olson and W. S. Owen, editors. *Martensite.* ASM International, Materials Park, OH, 1992.

[15] K. Otsuka and C. M. Wayman, editors. *Shape Memory Materials.* Cambridge University Press, Cambridge, 1998.

[16] R. Pego. Phase transitions in one-dimensional nonlinear viscoelasticity: Admissibility and stability. *Archive for Rational Mechanics and Analysis*, 97:353–394, 1987.

[17] M. Pitteri and G. Zanzotto. *Continuum theories for phase transitions and twinning in crystals.* Chapman and Hall, 2004.

[18] G. Puglisi and L. Truskinovsky. Thermodynamics of rate independent plasticity. *J. Mech. Phys. Solids*, 53:655–679, 2005.

[19] E. K. H. Salje. *Phase transitions in ferroelastic and co-elastic crystals.* Cambridge University Press, Cambridge, 1993.

[20] J. A. Shaw and S. Kyriakides. On the nucleation and propagation of phase transformation fronts in a NiTi alloy. *Acta Mater.*, 45:683–700, 1997.

[21] M. Slemrod. Admissibility criteria for propagating phase boundaries in a van der Waals fluid. *Archive for Rational Mechanics and Analysis*, 81:301–315, 1983.

[22] L. I. Slepyan. Feeding and dissipative waves in fracture and phase transition ii. phase-transition waves. *Journal of the Mechanics and Physics of Solids*, 49:513–550, 2001.

[23] L. I. Slepyan and L. V. Troyankina. Fracture wave in a chain structure. *Journal of Applied Mechanics and Technical Physics*, 25(6):921–927, 1984.

[24] L. Truskinovsky. Equilibrium interphase boundaries. *Soviet Physics Doklady*, 27:306–331, 1982.

[25] L. Truskinovsky. Dynamics of nonequilibrium phase boundaries in a heat conducting elastic medium. *J. Appl. Math. Mech.*, 51:777–784, 1987.

[26] L. Truskinovsky. Kinks versus shocks. In E. Dunn R. Fosdick and M. Slemrod, editors, *Shock Induced Transitions and Phase Structures in General Media*, volume 52 of *IMA*, pages 185–229. Springer-Verlag, 1993.

[27] L. Truskinovsky. About the "normal growth" approximation in the dynamic theory of phase transitions. *Continuum Mechanics and Thermodynamics*, 6:185–208, 1994.

[28] L. Truskinovsky and A. Vainchtein. Peierls-Nabarro landscape for martensitic phase transitions. *Physical Review B*, 67:172103, 2003.

[29] L. Truskinovsky and A. Vainchtein. The origin of nucleation peak in transformational plasticity. *Journal of the Mechanics and Physics of Solids*, 52:1421–1446, 2004.

[30] L. Truskinovsky and A. Vainchtein. Kinetics of martensitic phase transitions: Lattice model. *SIAM Journal on Applied Mathematics*, 66:533–553, 2005.

[31] L. Truskinovsky and A. Vainchtein. Quasicontinuum models of dynamic phase transitions. *Continuum Mechanics and Thermodynamics*, 18(1-2):1–21, 2006.